RADIATION DAMAGE TO RESISTIVE RANDOM ACCESS MEMORY

By

Kaiwen Hsu

A dissertation submitted in partial fulfillment of

the requirements for the degree of

Doctor of Philosophy

(Electrical and Computer Engineering)

at the

UNIVERSITY OF WISCONSIN-MADISON

2016

Date of final oral examination: 01/29/2015

The dissertation is approved by the following members of the Final Oral Committee:

Shohet, Juda. L, Professor, Electrical and Computer Engineering

Nishi, Yoshio, Professor, Electrical and Computer Engineering

Ma, Zhenqiang, Professor, Electrical and Computer Engineering

Hu, Yu Hen, Professor, Electrical and Computer Engineering

Mawst, Luke, Professor, Electrical and Computer Engineering

RADIATION DAMAGE TO RESISTIVE RANDOM ACCESS MEMORY

Kaiwen Hsu

Under the supervision of Professor J. L. Shohet

at the University of Wisconsin-Madison

ABSTACT

Resistive Random Access Memory (RRAM), is considered to be a very promising memory technology for the next generation of computer memory has undergone intense research in both industry and academia in the last ten years. As RRAM technology matures and electronic devices using RRAM are likely to be built soon, malfunctions of RRAM caused by cosmic rays and/or other radiation will become an important problem in industry since the size of these devices will continue to decrease. Of primary concern for RRAM are changes in performance and reliability of RRAM due to this radiation.

In order to determine the mechanism of the damage produced by irradiation, multiple diagnostics were used to measure the damage level on HfO_2 blanket films and two types of HfO_x RRAM cells before and after exposure to neutrons and protons. For HfO_2 blanket films,

electron-spin resonance (ESR) was used to detect defect-state concentrations before and after exposure. Leakage currents for irradiated HfO_2 films were measured. Changes to crystal structure were measured with an x-ray diffractometer (XRD). For HfO_x RRAM, forming process, I-V characteristics and endurance were examined before and after irradiation.

Displacement damage and followed by annealing effects from neutrons were observed with ESR and leakage current measurements on HfO_2 blanket films. 90% of HfO_x RRAM cells were formed and end up in the low-resistance state (LRS) under a high neutron fluence which infers neutrons create a conduction path by producing oxygen vacancies. Generation of oxygen vacancies is attributed to displacement damage by neutron irradiation. On the other hand, an observed increase in the resistance of the high resistance state (HRS) of RRAM may be attributed to an annealing effect.

For protons, only the annealing effect was observed from both ESR and leakage current measurements on HfO_2 blanket films. For proton-irradiated HfO_x RRAM, no forming were observed. However, a similar increase as in the case of neutron irradiation in the HRS was observed. Protons also annealed the HfO_x film within a RRAM as was also the case for neutron irradiation.

The changes in atomic-structure in HfO_2 films were investigated with XRD. The results showed the HfO_2 films become more crystalline after both neutron and proton irradiation. This

change results in shifts in values of the set voltage and degradation of endurance for both neutron-irradiated and proton-irradiated RRAM cells.

Based on these results, a modified RRAM configuration is proposed and was shown to be more resistant to neutrons and protons than the original RRAM configuration.

Acknowledgements

I would like to express my special appreciation and thanks to my advisor Professor. J. L. Shohet. You have been a tremendous mentor for me. I would like to thank you for encouraging my research and for allowing me to grow as a research scientist. Your advice on both research as well as on my career have been priceless. I would also like to thank my committee members, especially Professor Nishi at Stanford for his advice and willingness to meet with me and arranging a close collaboration with his students, Professor Ma, Professor Hu, and Professor Mawst for serving as my committee members even with my defense being held at noon. I also want to thank you for letting my defense be an enjoyable moment, and for your brilliant comments and suggestion.

I would like to thank Liang Zhao, and Ziwen Wang at Stanford University for providing me the RRAM cells. In addition, my sincerely thanks also goes to Dr. Tzu-hsuan Chang, who helped me to do the initial measurements on RRAM cells. Besides, a special acknowledgement goes to Robert J. Agasie, Tobey James Betthauser, Jerry Nickles, and Paul Ellison who provided me access and assistance at the facilities that allowed me to irradiate samples with neutrons and protons. All of you have been there to support me when I collected data for my Ph.D. thesis.

I must also acknowledge my fellow graduate students in the UW *Plasma Processing and Technology Laboratory*, Dongfei Pei, Weiyi Li, Huifeng Zhang, Josh Blatz, Faraz Choudhury and Ha Nguyen, who gave me lots of instructions on the practical operations and useful pieces of discussions during the experimental work. I really enjoyed the time to stay with you guys no matter at the 2nd floor old lab or the current lab in the basement.

A special thanks to my family. Words cannot express how grateful I am to my father, sisters, sister-in-law and Chun-Chou for all of the support from Taiwan. I would also like to thank Yiqian Lu who supported me and incentivized me to strive towards my goal.

At the end I would like express appreciation to my beloved husband Dr. Jen-Yung Chang who spent sleepless nights with and was always my support in the moments I needed help.

Table of Contents

Chapter 1 - Introduction

As the size of devices decreases and the complexity of electronic chips increases, cosmic-ray-induced crashes and/or radiation-induced damage are becoming a severe threat to electronic circuits and devices. Resistive Random Access Memory (RRAM),[1] which is considered as a very promising memory technology for embedded systems, has undergone intense research in both industry and academia in the last ten years. The advantage of a RRAM cell is because of its very simple structure: a layer of dielectric is "stacked" between two layers of metal and can be integrated with conventional CMOS fabrication technology.

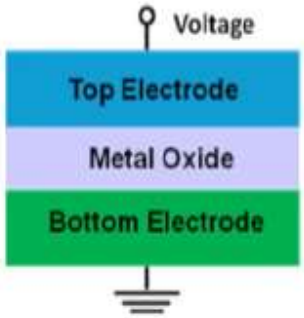

Figure 1. Schematic of RRAM cell in its simplest form. Adapted from [1].

As RRAM technology matures and electronic devices using RRAM are likely to be built, malfunctions of RRAM caused by cosmic rays and/or other radiation will become an important problem in industry since the size of these devices will continue to decrease. There are many effects produced by such radiation and they vary in magnitude from data disruptions to complete device failure. Of primary concern for RRAM is a change in resistance of the metal oxide since the two states of a RRAM memory cell depend on the resistance of the metal oxide. There is a consensus that the resistance change of the metal oxide is related to a change in the defect

concentration[2] present in the metal oxide. Therefore, we must first consider how radiation affects the defect concentration.

Thus, this work focuses on two specific issues: (1) how the radiation affects the properties of the metal oxide, and (2) permanent degradation in performance and reliability of RRAM due to radiation.

Much literature has discussed radiation effects on different RRAM cells. Earlier work showed that TiO_2 RRAM cells were tolerant to high levels of several radiation sources.[3,4,5] For TaO_2-based RRAM cells, they have shown various sensitivities to different radiation sources.[6,7]

In this work, we investigate the details of radiation-induced effects on HfO_2-based RRAM. A comparison of the effects induced by different radiation sources will be provided.

1.1 Purpose of This Work

The goal of this work is to investigate how cosmic rays and/or other radiation affects RRAM. The work determines the mechanisms that cause changes in states of a memory cell with concomitant permanent degradation in switching behavior. In addition, making RRAM becomes more damage resistant is also a goal of this work.

To proceed, this work will be divided into two parts. Part I will concentrate on blanket films. Typical metal oxides used for RRAM, especially HfO_2, will be deposited on Si substrates. These samples will be exposed to those species included in radiation that could be damaging: neutrons and protons. To detect the influence of these species, multiple diagnostics will be used. Electron-spin resonance (ESR) will be used to detect defect-state concentrations of the metal oxides deposited on high-resistivity substrates before and after exposure. Changes in leakage currents produced by radiation are also measured with a picoammeter. An x-ray diffractometer (XRD) will

also be utilized to measure changes in crystal structure. Analysis of the results will determine how the properties of these dielectrics are modified by radiation.

Part II will focus on RRAM. The radiation source and fluence will be the same as in Part I. The influence of radiation on RRAM, observed by examining the forming process, I-V characteristics and endurance, will be the key measurements in this part.

1.2 Outline of Thesis

This thesis is organized as follows. Chapter II provides background information on RRAM and details of the switching mechanisms. Cosmic rays and other radiation generated during plasma processing are described. Two fundamental mechanisms of radiation damage and radiation-induced effects will be discussed. Finally, detailed information will be provided on radiation-induced effects on different types of RRAM cells.

Chapter III describes the experimental apparatus that has been used in this work. Three exposure systems, (1) a nuclear reactor as a neutron source, (2) a linear particle accelerator, and (3) an ion implantation, are introduced. Two different fabrication process of the metal-insulator-metal RRAM structure are used in this analysis. They are: Type 1, a thick dielectric film produced by sputtering and Type 2, a thin dielectric film produced by atomic layer deposition (ALD). The techniques used to investigate damage on blanket films and RRAM cells are then discussed.

In Chapter IV, neutron-induced effects are shown. For effects on blanket films, electron-spin resonance is used to measure changes in defect concentration and I-V characteristics are measured to support the ESR data. X-ray diffraction is also used to detect changes in crystal structure by neutrons. The experimentally measured influence of radiation on RRAM, especially the forming process, I-V characteristics and endurance of a RRAM are also shown in this chapter. A thin-

oxide layer produced by ALD within a RRAM will be shown to be a potential design that can increase radiation hardness.

In Chapter V, proton-induced effects on the blanket film and RRAM are measured using the same techniques described in Chapter 4. A thin-oxide layer produced by ALD within a RRAM will also be shown to be a potential design that can increase radiation hardness.

Finally, Chapter VI includes a summary and comparison of the results drawn from this work and potential topics for future work.

REFERENCES

[1] H.-S. Philip Wong, H-Y Lee, S. Yu, Y. S. Chen, Y. Wu, P-S Chen, B. Lee, F. T. Chen, and M-J Tsai, "Metal–oxide RRAM," *Proc. IEEE* **100**, 1951 (2012).

[2] S. Yu, X. Guan, and H.-S. Philip Wong, "Conduction mechanism of TiN/HfO_x/Pt resistive switching memory: A trap-assisted-tunneling model," *Appl. Phys. Lett.* **99**, 063507 (2011).

[3] E. DeIonno, M. D. Looper, J. V. Osborn, H. J. Barnaby, and W. M.Tong, "Radiation effects studies on thin film TiO_2 memristor devices," *In Aerospace Conference IEEE* (2013).

[4] H. J. Barnaby, S. Malley, M. Land, S. Charnicki, A. Kathuria, B. Wilkens, E. DeIonno, and W. Tong, "Impact of alpha particles on the electrical characteristics of TiO memristors," *IEEE Trans. Nucl. Sci.* **58**, 2838 (2011).

[5] M. Vujisic, K. Stankovic, N. Marjanovic and P. Osmokrovic, "Simulated effects of proton and ion beam irradiation on titanium dioxide memristors," *IEEE Trans. Nucl. Sci.* **57**, 1798 (2010).

[6] F. Tan, R. Huang, X. An, Y. Cai, Y. Pan, W. Wu, H. Feng, X. Zhang and Y. Wang, "Investigation on the response of TaO-based resistive random-access memories to heavy-ion irradiation," *IEEE Trans. Nucl. Sci.* **60**, 4520 (2013).

[7] L. Zhang, R. Huang, D. Gao, P Yue, P. Tang, F. Tan, Y. Cai and Y. Wang, "Total ionizing dose (TID) effects on-based resistance change memory," *IEEE Trans. Electron Devices* **58**, 2800 (2011).

Chapter 2 - Background

In this Chapter, we introduce some background information for this work and separate it into four sections: (1) introduction to RRAM, (2) radiation sources and damage mechanisms, (3) changes in the properties of dielectrics used in RRAM produced by radiation, and (4) other studies of radiation-induced effects on RRAM. The material provided in this Chapter is important for understanding the work presented in subsequent chapters.

2.1 Introduction to RRAM

2.1.1 History, development, and applications

A RRAM cell is a metal oxide sandwiched between two metal electrodes, making what is called a metal-insulator-metal (MIM) structure. For proper operation, the oxide used in a MIM structure turns into a conductive state when a voltage is connected across it. This property has been known for over 40 years.[1]

Early observations of resistive switching were not robust enough for memory applications and these reports remained in the domain of scientific studies. The recent revival of interest in resistive switching began in the late 1990s, first with complex metal oxides such as the pervoskite oxides of $SrTiO_3$, $SrZrO_3$, and later the binary metal oxides such as NiO and TiO_2. Many companies started to develop memory with these simple switching elements, some of which became patented versions of RRAM.[2,3] Research activity began to intensify when Samsung released a paper at the International Electron Devices Meeting (IEDM) in 2004 that presented NiO memory cells integrated with conventional 0.18 μm complementary metal-oxide-semiconductor (CMOS) in a

one-transistor-one-resistor (1T1R) device structure.[4] Its memory-cell properties, as well as a more complete set of measurements for devices such as data retention, endurance and programming characteristics were reported. They suggested that a memory technology based on resistivity switching might be feasible. Extending the research to NiO RRAM, researchers at Fujitsu doped Ti into a NiO film to achieve low power and high-speed switching device properties.[5] At IEDM 2008, the highest performance RRAM technology was demonstrated by ITRI showing switching times less than 10 ns and currents less than 30 μA.[6] At IEDM 2010, an ultra-low energy consumption RRAM with good endurance and retention was shown. It is the first time that the switching energy of RRAM became close to that of existing flash memory.[7] Figure 1 shows the improvements of RRAM operation, speed and current.

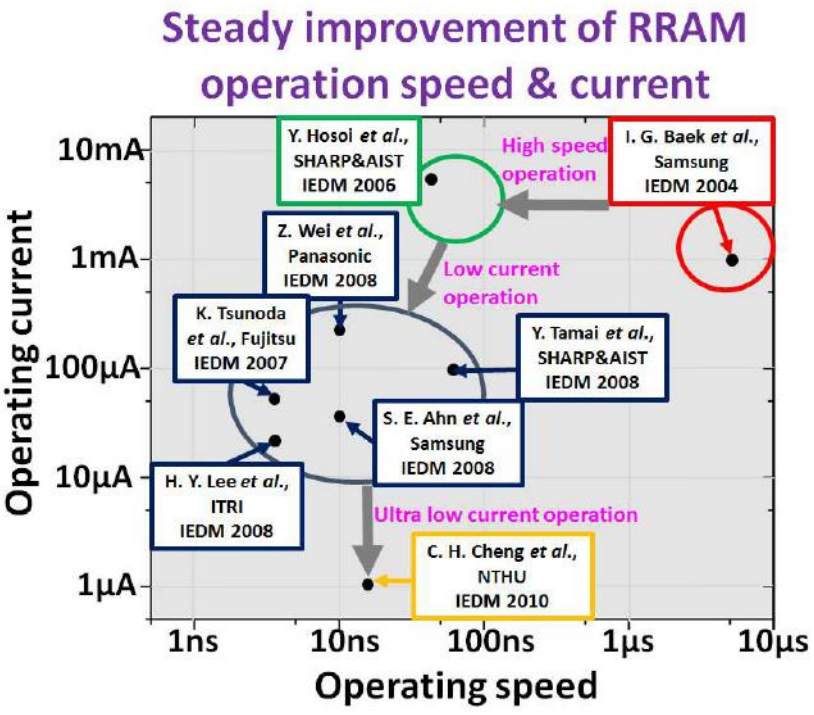

Figure1. Improvement of RRAM operation in term of speed and current.

Based on the improvements in operating current and speed, RRAM may now be suitable for embedded applications as well as for nonvolatile memory (NVM).[8] In addition to optimizing the operational speed and current, research has also focused on a new emerging-device structure. Figure 2 shows two structures of RRAM. As mentioned above, 1T-1R means a RRAM cell is connected to a transistor. 1D-1R means a RRAM cell is connected to a diode. These combinations allow these devices to function as memory.[9]

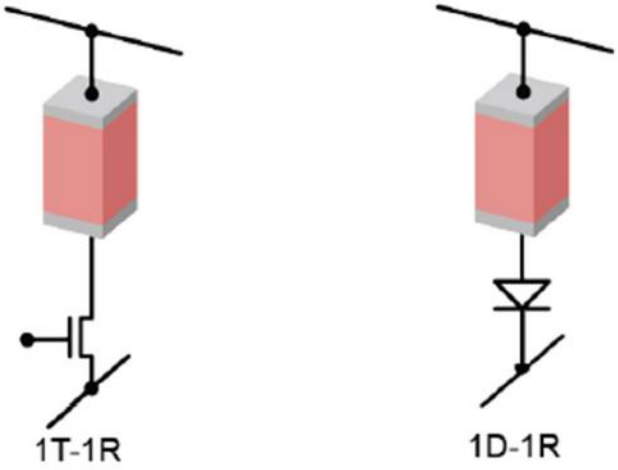

Figure 2. Two different device structures of RRAM. Adapted from [D. WOUTESR SISC 2012].

2.1.2 Resistive-switching mechanism

Like other memories, a RRAM has two different states: (1) a high-resistance state (HRS) and (2) a low-resistance state (LRS). Switching from HRS to LRS is called the set process, and the voltage needed to produce the set process is called the set voltage. Inversely, switching from LRS to HRS is called the reset process and the voltage needed to produce the reset is called the reset voltage. The switching can be broadly classified into two different modes: unipolar and bipolar. Figure 3 shows a sketch of the *I-V* characteristics for the two switching modes. Unipolar switching (a)

means the switching depends on the amplitude of the applied voltage and not on the polarity of the applied voltage. Thus, the set and reset can take place at the same voltage polarity. The bipolar switching mode (b) means the switch depends more on the polarity than the amplitude of the applied voltage. For the bipolar switching mode, set occurs at one polarity and reset occurs at the opposite polarity.

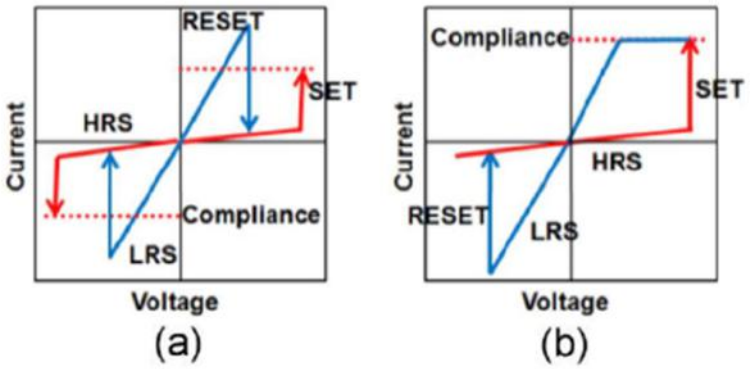

Figure 3. Two modes of operation: In the unipolar mode (a), the RRAM can switch between the HRS and LRS by using the set and reset voltage, which have the same polarity. In the bipolar mode (b), the RRAM can switch between the HRS and LRS by using set and reset voltages that are of opposite polarity. In addition, a method that limits the current during the set process must be used; otherwise, the RRAM will be burned out immediately. Adapted from [9].

At startup, the number of intrinsic defects in the metal oxide in a pristine RRAM cell is small.[9] A voltage higher than the set voltage is needed to create more defects for resistive-switching behavior. This is called the "electroforming" or "forming" process.[10] In this process, a high electric field (> 10 MV/cm) is applied across the oxide, resulting in oxygen ions leaving the lattices of the metal oxide and moving toward the anode. This localized deficiency of oxygen leads to the formation of conductive filaments (CFs). After this step, a significant number of defects are present.[11] In

subsequent switching cycles, only the set or reset voltages, which are smaller than the forming voltage, are needed to achieve the switching between HRS and LRS.

The set process can be interpreted to be a dielectric soft breakdown.[12] That is, the breakdown occurs along a conducting path in the metal oxide that is formed temporarily. Figure 4 shows some possible electron-conduction processes through the oxide material. The electrons will seek the least resistive paths among all the possibilities.

As a result, various metal-oxide RRAM cells may have different dominant conduction mechanisms depending on the dielectric properties, the fabrication process, and the properties of the interface between the oxide and the electrodes. For an HfO_2 RRAM, the conduction mechanism is dominated by defect-assisted tunneling.[13] The defects are composed of either oxide vacancies or metal precipitates. Determination of the conduction mechanisms for other metal oxides is still an active research area.

However, there is no current consensus about how the reset occurs.[9] It seems that a thermal-dissolution process[14] can explain parts of the unipolar switching characteristics, while an ion-migration process[15] can explain parts of the bipolar switching characteristics. During the reset process, which returns the memory to the HRS, oxygen ions migrate back to the bulk either to recombine with the oxygen vacancies or with metal precipitates in the oxide. In the thermal-dissolution mode, joule heating from the current thermally activates the diffusion of oxygen ions.[14] Oxygen ions diffuse from the interface or the region around the CFs. For the ion-migration mode, pure thermal diffusion is not sufficient, and therefore a reverse electric field is needed to aim the oxygen ions back to the bulk.[15]

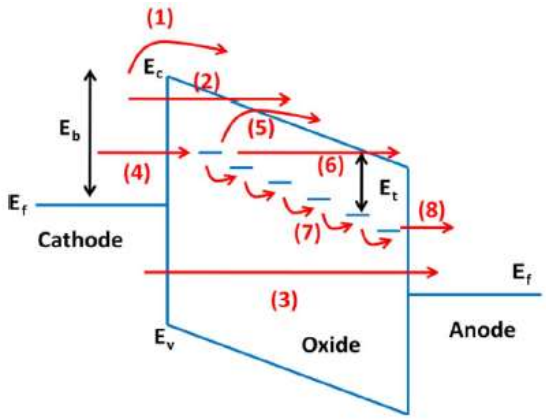

Figure 4. Schematic of possible electron conduction paths through a MIM stack. (1) Schottky emission (2) Fowler–Nordheim (F–N) tunneling (3) Direct tunneling (4) tunneling from cathode to traps; (5) Poole–Frenkel emission; (6) F–N-like tunneling from trap to conduction band; (7) trap-to-trap hopping or tunneling (8) tunneling from traps to anode. Adapted from [9].

Based on the above observations, Yu *et al.*[16] proposed a unified reset mechanism for both unipolar and bipolar modes. This work showed that for devices without an interfacial barrier such as those using a noble metal for the electrode, unipolar switching behavior is obtained. For devices with an interfacial barrier, which use an oxidizable metal as the electrode, bipolar switching behavior is obtained.[16]

2.1.3 Endurance and Retention

In this section, endurance and retention of RRAM are discussed. Endurance is the number of pulsed-voltage cycles that can be applied to a RRAM until it becomes unreliable. Typical pulsed-voltage cycles are shown in Figure 5. Retention for HRS and LRS is determined by how long the resistance of HRS and LRS can remain at their initial values.

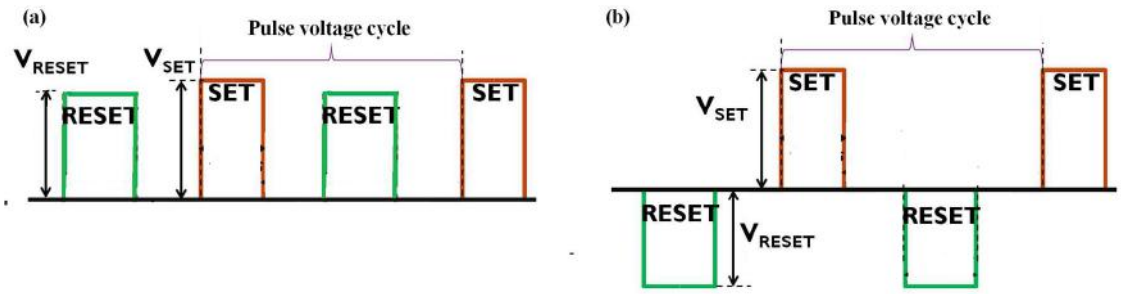

Figure 5. (a) Pulsed voltage cycle of unipolar switching mode, (b) Pulsed voltage cycle of bipolar switching mode.

There are few references that focus on the endurance and retention for RRAM. According to a paper published by Chen[17], endurance and retention failure can be discussed systematically. Endurance failure can be classified into two modes: set failure and reset failure. Figure 6 shows these two types of endurance failures.

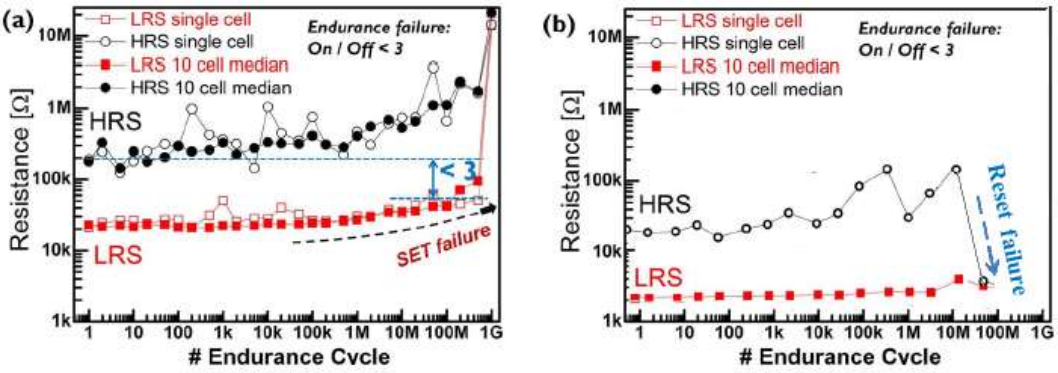

Figure 6. (a) Typical SET failure (b) Typical RESET failure. Adapted from [17].

For set failure, the resistance of the LRS of the memory tends to increase and finally it is not able to switch to the LRS. For reset failure, the resistance of the HRS of the memory tends to decrease and finally it is stuck in the LRS.

Retention failure can also be classified into two modes: HRS degradation and LRS degradation. For HRS degradation, the resistance of the HRS decreases with longer operation time and causes

retention failure. For LRS degradation, the resistance of the LRS increases with operation time and also causes failure.

2.2 Radiation Sources and damage mechanisms

2.2.1 Cosmic rays and other radiation

About 90% of cosmic rays are protons. The rest of the cosmic-ray composition consists of alpha particles, beta particles, neutrons, heavy ions and some photons (particularly x-ray and gamma ray).[18] The protons react with the earth's atmosphere via a strong interaction and produce complex cascades of secondary particles, such as protons, muons, neutrons and pions.[19, 20] Other radiation, such as vacuum ultraviolet (VUV), is often generated during plasma processing.[21]

2.2.2 Fundamental mechanisms of radiation damage

All of these particles and radiation described in previous section lose their energy via ionizing or nonionizing process as they travel through a given material. The result of this energy loss is the production of electron-hole pairs (ionization)[22] and displaced atoms (displacement damage).[23]

Ionization can be caused by charged particles, including the ones with energies too low to cause lattice effects. The ionization effects are usually transient, which might create "glitches" or single event upsets (SEUs)[24], but can also lead to destruction if they trigger other damage mechanisms.[25] Photocurrents caused by ultraviolet and x-rays can also be regarded as ionization damage.[22] Gradual accumulation of holes in the oxide layer may leads to worsening of device performance, up to device failure when the additional charge is high enough.[26]

For the displacement damage that is caused by neutrons, protons, heavy ions and very high-energy gamma-ray photons, the primary lattice defects created are vacancies and interstitials. A vacancy

is the absence of an atom from its normal lattice position. If the displaced atom moves into a nonlattice position, the resulting defect is called an interstitial. The interstitials here might be a result of a nuclear reaction. In other words, the whole displacement process includes several steps, such as high-energy particles interacting with the material, transmutation of atoms in the material[27], movement of atoms from their lattice structure, and formation of vacancies. An example of a collision and the resulting vacancies and interstitials is shown in Figure 7.[28] The combination of a vacancy and an adjacent interstitial is known as a Frenkel pair.[29]

Disturbances to the lattice's periodicity may give rise to energy levels in the bandgap. The energy levels in the bandgap might lead to thermal generation of electron-hole pairs, recombination of electron-hole pairs, trapping or production of majority and minority carriers, etc. The impacts of these effects depend on the working mechanisms of semiconductor and the nature of the radiation damage.[29]

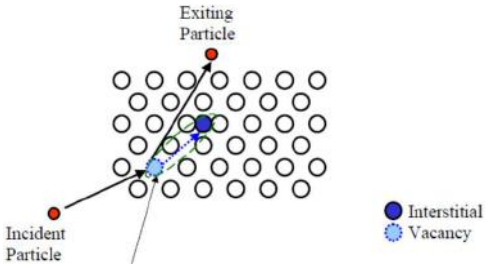

Figure 7. Displacement damage. Adapted from [28].

2.3 Changes in the properties of dielectrics used in RRAM produced by radiation

Ionization and displacement damage can affect dielectrics used in RRAM. In this section, we will describe two effects in dielectrics that are attributed to either ionization or displacement damage. These can affect the performance of RRAM.

2.3.1 Defect formation

The numbers of defects in both Si/SiO_2 and Si/HfO_2 systems can be modified by radiation, *e.g.* x-rays, gamma rays and VUV.[30,31,32] Usually, there is a very thin (~1nm) SiO_2 interfacial layer between the HfO_2 and the Si.[33] Thus, the same defects can be investigated in Si/SiO_2 and Si/HfO_2 systems.[32] In these references, electron-spin resonance (ESR) was used to detect defects in both Si/SiO_2 and Si/HfO_2 systems. In order to obtain effective ESR results, the SiO_2 and HfO_2 were deposited on high-resistivity substrates.[34]

The primary defects measured with ESR are Pb-type states and E' states. The Pb-type state is a trivalent center at the interface bonded to three Si atoms with a dangling orbital perpendicular to the interface. The two Pb-type defects on (100) silicon wafers are defined as Pb0 and Pb1.[35] The E' state is a positively charged oxygen vacancy.[36] At $\Theta = 0$ (B-field parallel to the sample normal), the Pb0, Pb1, and E' states were found to have g values of 2.0062, 2.0037, and 2.0002 respectively, which are typical values. [32]

According to the original ESR paper measuring the Pb and E' by Nishi[37], the influence of radiation on the Pb states and the E' states has been intensively studied.

2.3.1.1. Si/SiO_2 system

In the Si/SiO_2 system, several models exist that describe the radiation effects on these defect states.[38, 39]The most common effect is that the ionizing radiation interacts with SiO_2 and generates holes that result in interface-state formation.[39] In particular, Winokur *et al.*[40] used a pulsed e-beam and Hu[41] used x-rays as radiation sources to observe these effects. They have argued that the formation of interface states is related to holes generated by the specific radiation source in the

SiO_2 followed by diffusion of molecular hydrogen near the interface. Significant quantities of hydrogen as impurities in SiO_2 were liberated by radiation.[42]

2.3.1.2 Si/HfO_2 system

In the Si/HfO_2 system, Kang *et al.* [43] found that gamma rays generate a large amount of *negative* oxide charge in HfO_2. Thus, the radiation response of HfO_2 and SiO_2 films are different. The lack of holes in HfO_2 results in fewer generated interface states.[43]

2.3.2 Charge generation

Charge generation in dielectrics from VUV, x-rays, gamma rays, alpha particles, beta particles, neutrons and protons can be classified into two different kinds of mechanisms: (1) direct ionization: ionization by the incident particle itself and (2) indirect ionization: ionization by secondary particles created by nuclear reactions between the incident particle and the atoms. In the following section, each type of ionization will be described in detail.

2.3.2.1 Direct Ionization

When energetic particles pass through a semiconductor or an insulating material, they can pass their energy to the electrons in that material and strip electrons from an electron shell of an atom, which leaves the atom with a net positive charge. This process is called direct ionization. VUV, x-rays, gamma rays, alpha particles, beta particles and protons can produce direct ionization when they interact with materials.[44,45,46] The radiation ionization energy as a function of band gap energy is shown in Figure 8. It can be seen that the ratio of radiation ionization energy to the band-gap energy is independent of the material.[47]

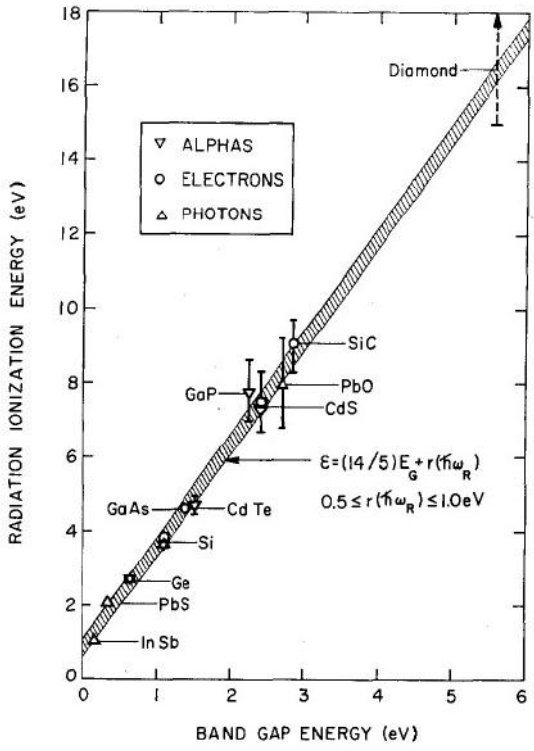

Figure 8. Radiation ionization energy as a function of band-gap energy. Adapted from [47].

Photons such as VUV, x-rays, and gamma rays can all transfer energy to the electrons in materials and cause photoemission. Sinha *et al.*[44] demonstrated how VUV generates charge in dielectrics. In addition, the excitation of electrons by x-rays is a very important property that generates x-ray electron photoemission spectra.[45] Photoemission is the dominant energy transfer mechanism for x-ray and gamma-ray photons with energies below 50 keV, but it is much less important for gamma rays at higher energies.[46] Alpha particles, beta particles and protons, which are charged particles themselves, can transfer their energy to electrons in materials by electromagnetic interaction[48] and cause direct ionization.

2.3.2.2 Indirect Ionization

Protons and neutrons can interact with chip materials and can cause emission of alpha particles, gamma rays or other particles along with the recoil of a daughter nucleus all of which may cause ionization. This indirect ionization is very important in terms of neutrons. Since neutrons are not charged particles, this is the main ionization mechanism of neutrons in materials. Figure 9 shows some of the nuclear reactions between protons with hafnium and oxygen nuclei. [49,50] Figure 10 shows some of the reaction products produced when a neutron interacts with hafnium and oxygen.[51]

Reaction Products For p + ^{16}O		Reaction Products For p+ ^{178}Hf and p+ ^{180}Hf	
Reaction Product			Reaction Product
$\alpha + {}^{13}N$		p+ ^{178}Hf	3n+α+^{172}Lu
p'+α+^{12}C			2n+α+^{173}Lu
2p+^{15}N			3n+t+^{173}Hf
			n+t+^{175}Hf
			n+^{177}Ta
		p+ ^{180}Hf	5n+α+^{172}Lu
			4n+α+^{173}Lu
			3n+t+^{175}Hf
			3n+^{177}Ta

Figure 9. Nuclear reactions between a proton with hafnium and oxygen nuclei.

Reaction Products For n+ ^{16}O		Reaction Products For n+ ^{178}Hf and n+ ^{180}Hf	
Reaction Product			Reaction Product
p+^{16}N		n+ ^{178}Hf	p+^{178}Lu
d+ ^{15}N			α+^{175}Yb
t+^{14}N		n+ ^{180}Hf	p+^{180}Lu
α+^{13}C			α+^{177}Yb

Figure10. Nuclear reactions between a neutron with a hafnium and an oxygen nucleus.

The amount of generated charge due to direct and indirect ionization is a function of the linear energy transfer (LET) rate, *i.e.*, the amount of energy released by a particle in a given material per unit distance travelled. The LET is dependent on the mass and energy of the particle and the material in which it is traveling. Typically, massive and energetic particles incident on dense materials have the highest LETs.[52]

2.4 Other studies of radiation-induced effects on RRAM

Presently, much literature focuses on radiation damage to resistive random-access memory. For TiO_x, TaO_x, and HfO_x RRAM, radiation effects have been studied with various sources.[53-59]

2.4.1 TiO_2 RRAM

For the TiO_2 RRAM, References [53] and [54] provide a review of different radiation effects. The radiation sources used included gamma rays, bismuth ions, protons, alpha particles and neutrons. In all cases, except for alpha particles, irradiation above a certain threshold (between 10^{14} and 10^{15} particles/cm^2), there was virtually no change in the resistances of the HRS and LRS. That was evidenced by the fact that the switching behavior doesn't change after irradiation. These works showed TiO_2 RRAM cells are tolerant to a number of radiation sources and seem to be suitable for space application.

2.4.2 TaO_x RRAM

For the TaO_x RRAM in Ref.[55], it was found that the LRS of RRAM is immune to gamma rays, whereas the sensitivity of the HRS to gamma rays depends on the dimensions of the devices, including the thickness of the oxide film and the area of the device. The HRS of a device with a large area and a thick oxide is vulnerable to gamma rays and has a high probability to change into

the LRS. To see this, note that it was assumed there are more trapped holes in the thicker oxide. These trapped holes may form a path for electron transport. For displacement damage caused by bromine ion bombardment, the resistance of the HRS was also found to be very sensitive to heavy-ion radiation. Some irradiated devices even changed from the HRS into LRS[56]. These results indicated that TaO_x-based RRAM need to be carefully designed for operation in a radiation environment.

2.4.3 HfO_2 RRAM

For the HfO_2 RRAM in Ref.[57], the resistive elements were shown to be tolerant against a total ionizing dose up to several Mrad of 10 keV x-rays. Excess carriers generated in the HfO_2 layer recombine or are trapped at defect sites in the HfO_2 layer or at interfaces between layers.[58] Fortunately, they have no effects on the HRS and LRS values. However, 1.8 MeV proton irradiation caused an increase in HRS resistance.[59] A scatter plot of the resistance vs proton fluence for several HfO_2-based RRAM cells is shown below. Fortunately, the logic state of the RRAM was not changed by proton irradiation.

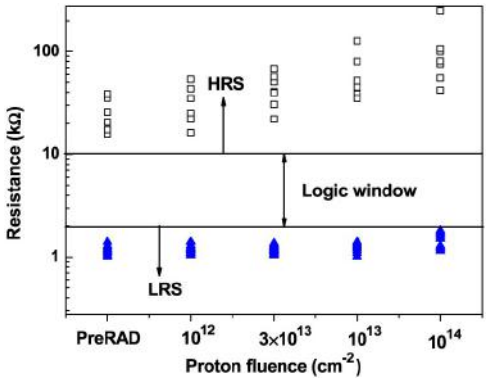

Figure12. Resistance of HRS and LRS as a function of proton fluence. Adapted from [59].

In addition, the set process for a HfO_2 based RRAM before and after exposure to proton is shown in Figure 13. The resistance of the RRAM was increased at a proton exposure level of 10^{14} cm^{-2} and the set voltage increases. It is more difficult to switch.

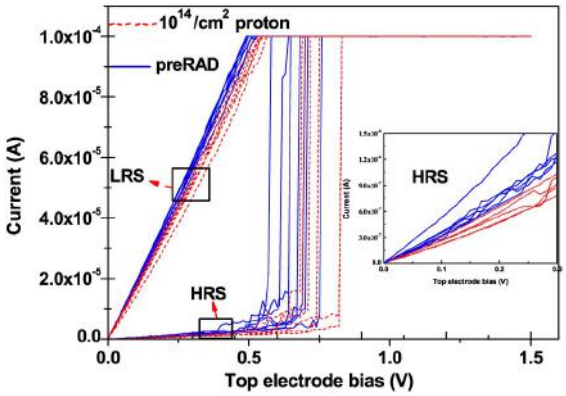

Figure13. Switching curve for a HfO_2/Hf-based RRAM before and after expose to 1.8 MeV proton. Adapted from [59].

REFERENCES

[1] P. H. Nielsen, N. M. Bashara, " The reversible voltage-induced initial resistance in the negative resistance sandwich structure," *IEEE Trans. Electron Devices* **11**, 243 (1964).

[2] Moon-Sook Lee and In-Gyu Baek, U.S. Patent 7,292,469

[3] K. A. Campbell, J. T. Moore, and T. L. Gilton, U.S. Patent 6,867,996

[4] I. G. Baek, M. S. Lee, S. Seo, M. J. Lee, D. H. Seo, D. S. Suh, J. C. Park, S. O. Park, H. S. Kim, I. K. Yoo, U. In. Chung and J. T. Moon, " Highly scalable nonvolatile resistive memory using simple binary oxide driven by asymmetric unipolar voltage pulses," *Tech. Dig. IEEE Int. Electron Devices Meeting*, 587 (2004).

[5] K. Tsunoda, K. Kinoshita, H. Noshiro, Y. Yamazaki, T. lizuka, Y. Ito, A. Takahashi, A. Okano, Y. hSato, T. Fukano, M. Aoki and Y. Sugiyama, "Low power and high speed switching of Ti-doped NiO ReRAM under the unipolar Voltage Source of less than 3V," *Tech. Dig. IEEE Int. Electron Devices Meeting*, 767 (2007).

[6] H. Y. Lee, P. S. Chen, T.Y. Wu, Y. S. Chen, C. C. Wang, P. J. Tzeng, C. H. Lin, F. Chen, C.H. Lien and M,-J. Tsai, " Low power and high speed bipolar switching with a thin reactive Ti buffer layer in robust HfO_2 based RRAM," *Tech. Dig. IEEE Int. Electron Devices Meeting*, 1 (2008).

[7] C. H. Cheng, C. Y. Tsai, A. Chin and F. S. Yeh, "High performance ultra-low energy RRAM with good retention and endurance," *Tech. Dig. IEEE Int. Electron Devices Meeting*, 448 (2010).

[8] In-Gyu Baek, RRAM technology from an industrial perspective, WWW Document (http://www.sematech.org/meetings/archives/fep/9064/Pres/19%20I-G%20Baek.pdf)

[9] H.-S. Philip Wong, H-Y Lee, S. Yu, Y. S. Chen, Y. Wu, P-S Chen, B. Lee, F. T. Chen, and M-J Tsai, "Metal–oxide RRAM," *Proc. IEEE* **100**, 1951 (2012).

[10] J. J. Yang, F. Miao, M. D. Pickett, D. A. Ohlberg, D. R., Stewart, C. N. Lau and R. S.Williams, "The mechanism of electroforming of metal oxide memristive switches," *Nanotechnology* **20**, 215201(2009).

[11] G. Bersuker, D. C. Gilmer, D. Veksler, P. Kirsch, L. Vandelli, A. Padovani, L. Larcher, K. Mckenna, A. Shluger, V. Iglesias, M. Porti and M. Nafria, " Metal oxide resistive memory switching mechanism based on conductive filament properties," *J. Appl. Phys.* **110**, 124518 (2011).

[12] N. Xu, L. Liu, X. Sun, X. Liu, D. Han, Y. Wang, R. Han, J. Kang and B.Yu, " Characteristics and mechanism of conduction/set process in TiN⁄ ZnO⁄ Pt resistance switching random-access memories," *Appl. Phys. Lett.* **92**, 232112 (2008).

[13] S. Yu, X. Guan, and H.-S. Philip Wong, "Conduction mechanism of TiN/HfO_x/Pt resistive switching memory: A trap-assisted-tunneling model," *Appl. Phys. Lett.* **99**, 063507 (2011).

[14] U. Russo, D. Ielmini, C. Cagli, A. L. Lacaita, S. Spiga, C. Wiemer, M. Perego and M. Fanciulli, " Conductive-filament switching analysis and self-accelerated thermal dissolution model for reset in NiO-based RRAM," *Tech. Dig. IEEE Int. Electron Devices Meeting*, 775 (2007).

[15] B. Gao, S. Yu, N. Xu, L. F. Liu, B. Sun, X. Y. Liu, R. Q. Han, J. F. Kang, B. Yu and Y.Y. Wang, " Oxide-based RRAM switching mechanism: A new ion-transport-recombination model," *Tech. Dig. IEEE Int. Electron Devices Meeting*, 563 (2008).

[16] S. Yu and H.-S. Philip Wong, "A phenomenological model for the reset mechanism of metal oxide RRAM," *IEEE Electron Device Lett.* **31**, 1455 (2010).

[17] Y. Y. Chen, R. Degraeve, S. Clima, B. Govoreanu, L. Goux, A. Fantini, G. S. Kar, G. Pourtois, G. Groeseneken, D. J. Wouters , "Understanding of the endurance failure in scaled HfO_2-based 1T1R RRAM through vacancy mobility degradation," *Tech. Dig. IEEE Int. Electron Devices Meeting*, 20 (2012).

[18] Thomas K. Gaisser, Cosmic rays and particle physics, pp. 1-11.

[19] J. F. Ziegler and W. A. Lanford, "The effect of sea level cosmic rays on electronic devices," *J.Appl. Phys.* **52**, 4305 (1981).

[20] J. L. Barth, C. S. Dyer, and E. G. Stassinopoulos, "Space, atmospheric, and terrestrial radiation environments," *IEEE Trans. Nucl. Sci.* **50** 466 (2003).

[21] H. Ren, G.A. Antonelli, Y. Nishi and J.L. Shohet, "Plasma damage effects on low-k porous organosilicate glass," *J. Appl. Phys.* **108**, 094110 (2010).

[22] H. Ren, H. Sinha, A. Sehgal, M.T. Nichols, G.A. Antonelli, Y. Nishi and J. L.Shohet, "Surface potential due to charge accumulation during vacuum-ultraviolet exposure for high-k and low-k dielectrics," *Appl. Phys. Lett.* **97**, 072901 (2010).

[23] *Radiation hardening* , WWW Document (http:// en.wikipedia.org/wiki/Radiation_hardening)

[24] T. C. May and M. H. Woods, "Alpha-particle-induced soft errors in dynamic memories," *IEEE Trans. Electron Devices* **26**, 2 (1979).

[25] T. Hirao, H. Itoh, S. Okada, I. Nashiyama, "Studies of single-event transient current induced in GaAs and Si diodes by energetic heavy ions," *Radiat. Phys. and Chem.* **60**, 269 (2001).

[26] G.Cellere, A. Paccagnella, "Subpicosecond conduction through thin SiO2 layers triggered by heavy ions," *J. Appl. phys.* **99**, 074101 (2006).

[27] *Nuclear transmutation*, WWW Document (https://en.wikipedia.org/wiki/Nuclear_transmutation)

[28] *Radiation effects and damage*, WWW Document (http://holbert.faculty.asu.edu/eee560/RadiationEffectsDamage.pdf)

[29] J. R. Srour, C. J. Marshall, and Paul W. Marshall, "Review of displacement damage effects in silicon devices," *IEEE Trans. Nucl. Sci.* **50**, 653 (2003).

[30] B. B. Triplett, T. Takahashi and T. Sugano, "Electron spin resonance observation of defects in device oxide damaged by soft x rays," *Appl. Phys. Lett.* **50**, 1663 (1987).

[31] P. M. Lenahan and P. V. Dressendorfer, "Hole traps and trivalent silicon centers in metal/oxide/silicon devices," *J. Appl. Phys.* **55**, 3495 (1984).

[32] H. Ren, S.L. Cheng, Y. Nishi and J.L. Shohet, "Effects of vacuum ultraviolet and ultraviolet irradiation on ultrathin hafnium-oxide dielectric layers on (100) Si as measured with electron-spin resonance," *Appl. Phys. Lett.* **96**, 192904 (2010).

[33] P. D. Kirsch, M. A. Quevedo-Lopez, H. J. Li, Y. Senzaki, J. J. Peterson, S. C. Song, S. A. Krishnan, N. Moumen, J. Barnett, G. Bersuker, and P.Y.Hung, "Nucleation and growth study of atomic layer deposited HfO_2 gate dielectrics resulting in improved scaling and electron mobility," *J. Appl. Phys.* **99**, 3508 (2006).

[34] M. Tabib-Azar, D. Akinwande, G. E. Ponchak, and S. R. LeClair, "Evanescent microwave probeson high-resistivity silicon and its application in characterization of semiconductors," *Rev. Sci. Instrum.* **70**, 3083 (1999).

[35] E. H. Poindexter, P. J. Caplan, B. E. Deal, and R. R. Razouk, "Interface states and electron spin resonance centers in thermally oxidized (111) and (100) silicon wafers," *J. Appl. Phys.* **52**, 879 (1981).

[36] S. Agnello, R. Boscaino, G.Buscarino, M.Cannas and F. M. Gelardi, "Structural relaxation of E_{r}' centers in amorphous silica," *Phys. Rev. B* **66**, 113201 (2002).

[37] Y. Nishi, "Study of Silicon-Silicon Dioxide Structure by Electron Spin Resonance I," *Jpn. J. Appl. Phys.* **10**, 52 (1971).

[38] Y. Y. Kim, P. M. Lenahan, " Electron-spin-resonance study of radiation-induced paramagnetic defects in oxides grown on (100) silicon substrates," *J. Appl. Phys.* **64**, 3551 (1988).

[39] Lenahan, P. M., and J. R. Conley Jr, "A comprehensive physically based predictive model for radiation damage in MOS systems," *IEEE Trans. Nucl. Sci.* **45**, 2413 (1998).

[40] P. S. Winokur, H. E Boesch, JL, Jo Mo McGarrity, and E So McLean, "Two-stage process for buildup of radiation-induced interface states," *J. Appl. Phys.* **50**, 3492 (1979).

[41] G. J. Hu and W. C. lohnson, "Relationship between x-ray-produced holes and interface states in metal-oxide-semiconductor capacitors," *J. Appl. Phys.* **54**, 1441 (1983).

[42] K. L. Brower, P. M. Lenahan, and P. V. Dressendorfer, "Defects and impurities in thermal oxides on silicon," *Appl. Phys. Lett.* **41**, 251(1982).

[43] A. Y. Kang, P. M. Lenahan and J. F. Conley, " The radiation response of the high dielectric-constant hafnium oxide/silicon system," *IEEE Trans. Nucl. Sci.* **49**, 2636 (2002).

[44] H. Sinha, H. Ren, M. T. Nichols, J.L. Lauer, M. Tomoyasu, N. M. Russell, G. Jiang, G. A. Antonelli, N.C. Fuller, S.U. Engelmann, Q.Lin, V. Ryan, Y. Nishi, and J. L. Shohet,"The effects of vacuum ultraviolet radiation on low-k dielectric films," *J. Appl. Phys.* **112**, 111101(2012).

[45] *X-ray photoelectron spectroscopy*, WWW Document (http://en.wikipedia.org/wiki/X-ray_photoelectron_spectroscopy)

[46] *Gamma ray*, WWW document (http://en.wikipedia.org/wiki/Gamma_ray)

[47] C. A. Klein, "Bandgap dependence and related features of radiation ionization energies in semiconductors," *J. Appl. Phys.* **39**, 2029(1968).

[48] *Electromagnetism*, WWW Document (http://en.wikipedia.org/wiki/Electromagnetic_force)

[49] S. Takács, F. Tárkányi, A. Hermanne and R. A. Rebeles, "Activation cross sections of proton induced nuclear reactions on natural hafnium," *Nucl. Instrum. Methods Phys. Res., Sect. B* **269**, 2824(2011).

[50] R. Chapman and A. M. Macleod, " Proton nuclear reaction cross sections in oxygen and neon at 13 MeV," *Nucl. Phys. A* **94**, 313 (1967).

[51] *Evaluated nuclear data file(ENDF) retrieval &plotting*, WWW Document (http://www.nndc.bnl.gov/sigma/index.jsp?as=28&lib=endfb7.1&nsub=10)

[52] R. C. Baumann, "Radiation-induced soft errors in advanced semiconductor technologies," *IEEE Trans. Device Mater. Rel.* **5**, 305 (2005).

[53] W. M. Tong, J. J. Yang, P. J. Kuekes, D. R. Stewart, R. S. Williams, E. DeIonno, E. E. King, S. C. Witczak, M. D. Looper, and J. V. Osborn, "Radiation hardness of memristive junctions," *IEEE Trans. Nucl. Sci.* **57**, 1640 (2010).

[54] E. DeIonno, M. D. Looper, J. V. Osborn and J. W. Palko, "Displacement damage in TiO_2 memristor devices," *IEEE Trans. Nucl. Sci.***60**, 1379 (2013).

[55] L. Zhang, R. Huang, D. Gao, P. Yue, P. Tang, F. Tan, Y. Cai, and Y. Y. Wang, "Total ionizing dose (TID) effects on-based resistance change memory," *IEEE Trans. Electron Devices* **58**, 2800 (2011).

[56] F. Tan, R. Huang, X. An, Y. Cai, Y. Pan, W. Wu, H. Feng, X. Zhang and Y. Y.Wang, "Investigation on the response of TaO_x-based resistive random-access memories to heavy-ion irradiation," *IEEE Trans. Nucl. Sci.* **60**, 4520(2013).

[57] S. L. Weeden-Wright, W. G. Bennett, N. C. Hooten, E. X. Zhang, M. W. McCurdy, M. P. King, R. A. Weller, M. H. Mendenhall, M. L. Alles, D. Linten, M. Jurczak, R. Degraeve, A. Fantini, R. A. Reed, D. M. Fleetwood and R. D. Schrimpf, "TID and displacement damage resilience of 1T1R resistive memories," *IEEE Trans. Nucl. Sci.* **61**, 2972 (2014).

[58] H. Ren, S. L. Cheng, Y. Nishi, and J. L. Shohet, "Effects of vacuum ultraviolet and ultraviolet radiation on ultrathin hafnium-oxide dielectric layers on (100)Si as measured with electron spin resonance," *Appl. Phys. Lett.* **96**, 192904 (2010).

[59] J. S. Bi, Z. S. Han, E. X. Zhang, M. W. McCurdy, R. A. Reed, R. D. Schrimpf, D. M. Fleetwood, M. L. Alles, R. A. Weller, D. Linten, M. Jurczak and A. Fantini, "The impact of x-ray and proton irradiation on HfO_2/Hf-based bipolar resistive memories," *IEEE Trans. Nucl. Sci.* **60**, 4540 (2013).

Chapter 3 - Experimental Apparatus

This chapter focuses on the experimental apparatus that will be used in this work. The process flow of the work includes four steps: (1) neutron and proton exposure, (2) fabrication process of Metal-Insulator-Metal (MIM) structures, (3) property measurements of blanket films, and (4) property measurements of RRAM devices. Exposure from several radiation sources will be made on both the blanket films and RRAM devices. Multiple diagnostics will be used to determine the changes in the films and devices.

3.1 Exposure systems

Three exposure systems are used in this work. They are: (1) a nuclear reactor, (2) a linear particle accelerator, and (3) ion implantation. The nuclear reactor generates a continuous neutron spectrum including neutrons with different energies. The linear particle accelerator generates 5MeV protons, and the ion implantation implants 60 keV protons. More detail about how the appropriate proton sources and energies were chosen is described in Chapter 5.

3.1.1 Nuclear reactor

The neutrons used in this work are generated at the Max Carbon Radiation Science center at the University of Wisconsin-Madison. This light-water-moderated nuclear reactor [1] has multiple irradiation facilities including:

(1) Three whale tubes: hydraulically operated in core.

(2) Pneumatic tubes: pneumatically operated in-core tubes with send and receive stations located in a fume hood; operated with carbon dioxide cover gas.

(3) Beam ports: 6” diameter in-core section with 8” diameter tube penetrating through the shield; equipped with lead shutters.

(4) Thermal columns: graphite filled irradiation space.

Figure 1 is view of the light-water-moderated nuclear reactor. The reactor pit is made of reinforced concrete.

Figure 1. UW Nuclear Reactor (UWNR) view from beam port floor.

The UWNR 1-MW-thermal nuclear reactor has a continuous neutron spectrum including thermal (<1eV), epithermal (> 1eV and < 1 MeV), and fast (>1 MeV) neutrons.

The data for exposures is shown in Table I. The power and exposure time are the main parameters that control the neutron fluence.

Power	Time	Fluence [n/cm^2]		
		Thermal (<1eV)	Epithermal (>1eV, <1MeV)	Fast (>1MeV)
1 W	3 s	1.33E+07	3.84E+05	1.76E+06
10 W	3 s	1.33E+08	3.84E+06	1.76E+07
100 W	3 s	1.33E+09	3.84E+07	1.76E+08
1000 W	3 s	1.33E+10	3.84E+08	1.76E+09
1.00E+04 W	3 s	1.33E+11	3.84E+09	1.76E+10
1.00E+05 W	3 s	1.33E+12	3.84E+10	1.76E+11
1.00E+06 W	3 s	1.33E+13	3.84E+11	1.76E+12
1.00E+06 W	30 s	1.33E+14	3.84E+12	1.76E+13
1.00E+06 W	300 s	1.33E+15	3.84E+13	1.76E+14

Table I. Exposure conditions used in this work.

3.1.2 Linear particle accelerator

Five MeV protons used in this work are generated using the tandem particle accelerator[2] at the University of Wisconsin-Madison Waisman Center. The accelerator is a National Electrostatics Corporation 9SDH-2 Electrostatic Tandem. It is shown in Figure 2. In this accelerator, > 100 uA of protons can be accelerated to 7 MeV. A magnet is used to control the beam shape and direction. The measurement of the beam current on samples is used to calculate the proton flux.

Figure 2. National Electrostatics Corporation 9SDH-2 electrostatic tandem to accelerate charged particles.

3.1.3 Ion implantation

The 60 keV proton implantation of the blanket films and RRAM was performed by Luxience Technology. The protons are electrostatically accelerated to this particular energy. The decision to implant at the energy of 60 keV will be discussed in Chapter 5.

3.2 Fabrication process of the Metal-Insulator-Metal (MIM) Structure

In this thesis, the RRAM cells are a TiN/HfO_2/Pt combination. Two fabrication processes for the RRAM cells are used.

For the Type 1 RRAM, the bottom electrode of Pt (~90 nm) is deposited by e-beam evaporation on a Si wafer with a 2-nm Ti adhesion layer. Then, HfO_x and TiN (~200 nm) are deposited by reactive sputtering at room temperature, followed by a lift-off process to generate a pattern on the top electrode.

For the Type 2 RRAM, the Pt bottom electrode (~40 nm) is first deposited by e-beam evaporation with 100-nm thermal-oxide adhesion layer. Then, a lift-off process is used to form 5-nm of atomic-layer-deposited (ALD) HfO_x, followed by deposition of a 70-nm reactive-ion sputtered TiN layer, patterned by lift-off.

3.3 Measurement of Dielectric Properties

Three types of dielectric properties were measured. They are: (1) defect-state concentration, (2) leakage current and (3) crystal structure.

3.3.1 Electron-Spin Resonance Spectroscopy (ESR)

ESR spectroscopy is used to measure defect-state concentration. The basic concept of ESR is that defect states (unpaired electrons) in a magnetic field absorb and emit electromagnetic radiation. Every electron has a magnetic moment and spin quantum number s=1/2, with magnetic components m_s=+1/2 and m_s=-1/2. The energy state of an electron can be represented as $E = m_s g\mu_B B_0$, where g is the g-factor, and μ_B is the Bohr magneton. For an unpaired electron, it can move between the two energy states by absorbing or emitting a photon. Hence, the fundamental equation for ESR spectroscopy is

$$h\nu = g\mu_B B_0. \quad (1)$$

In this case, the microwave frequency and the magnetic field value are two parameters that can be varied. Thus there are many of combinations of frequency and magnetic field values that yield the same energy. In common ESR systems, the frequency is usually located in the 9-10 GHz region, with a corresponding magnetic field at 3500 G. In our system, the frequency is fixed during measurement and a scan of the magnetic field is used to match the absorption or emission energy of the photons to satisfy equation (1).

Figure 3 shows a conventional ESR system that includes the magnets, the microwave source, and the detection system. The dielectric sample is placed in the resonant cavity in the magnet and the electromagnetic energy is coupled from the microwave source into the cavity so that ESR spectra can be obtained from the detecting system. The ESR measurements were performed at room temperature using a Bruker EleXsys E500 spectrometer working at a frequency of ~ 9.85 GHz. The resistivity of the silicon substrate is 4000 Ω·cm. This high resistivity is needed to obtain

effective ESR measurements. A 0.0003% KCl weak-pitch sample (3.7×10^{13} spins/cm) was used to calibrate the system.

To analyze the ESR signal and identify defect states, the following steps are used. First, the ESR signal can be regarded as the summation of the signals of several major defect states. The equation for the signal amplitude can therefore be expressed as a linear combination of defect state signals as shown in equation (2).

$$I_{ESR} = \sum I_i(B) \tag{2}$$

I_{ESR} is the ESR signal and I_i is the signal for the ith defect state. The signal strength varies with the external magnetic field B. The value for $Ii(B)$ is obtained by doing a least-squares fit of the data to equation (2). For material with a crystal structure, the Broer model[3] was used to investigate the defect behavior during ESR measurements. This model was developed based on the response of the defects to the local magnetic field. Each defect has its fingerprint, i.e. its g-factor, which depends on the microwave frequency and magnetic field strength as

$$g = \frac{h\nu}{\mu_B B_0} \tag{3}$$

where h is Planck's constant, μ_B is the Bohr magneton $eh/(4\pi m_e)$, ν is the frequency of the oscillating microwave field, and B_0 is the magnetic field strength at the peak of ESR absorption for each defect. The g-factor for a free unpaired electron is 2.0023193. For a defect (unpaired electron bonded to a particular electronic structure), the g factor deviates from this value because of the interactions in the electronic structure.

In this model, $Ii(B)$ has the form of the derivative of a Gaussian

$$Ii(B)=-\frac{2A_{i0}(B-B_{i0})}{\sigma_i^2}e^{-\frac{(B-B_{i0})^2}{\sigma_i^2}} \quad (4)$$

where A_{i0}, B_{i0}, and σ_i are parameters found during the least-squares fitting process because multiple defects can overlap to form the net signal. A_{i0} is the amplitude and σ_i is the B-field width.

The relative concentration of each defect can be calculated by integrating the area under the absorption line to yield

$$C_{ir}=\int_{B_{low}}^{B_{high}} A_{io}\, e^{-\frac{(B-B_{i0})^2}{\sigma_i^2}}\, dB \approx \sqrt{\pi}A_{i0}\sigma_i \quad (5)$$

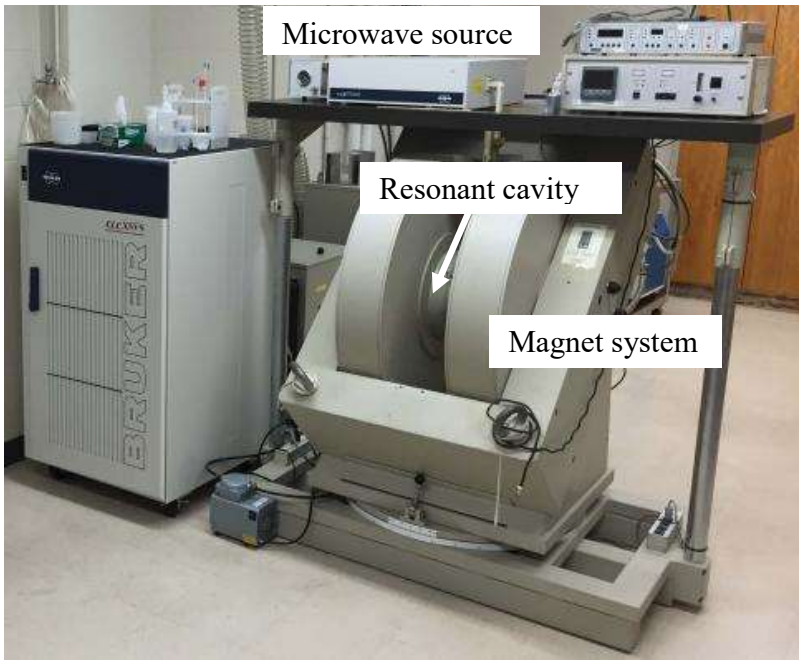

Figure 3. Photograph of the x-band ESR system.

3.3.2 I-V Characteristics

Metal-insulator-semiconductor (MIS) structures were fabricated on the dielectric films to measure leakage currents. Electrode patterns for the MIS structure were defined using commercially available transmission electron microscope (TEM) grids as masks. The TEM grids used for this

purpose are made of nickel and have an array of hexagonal patterns. An optical micrograph of the structure formed by the TEM grid is show in Figure 4.

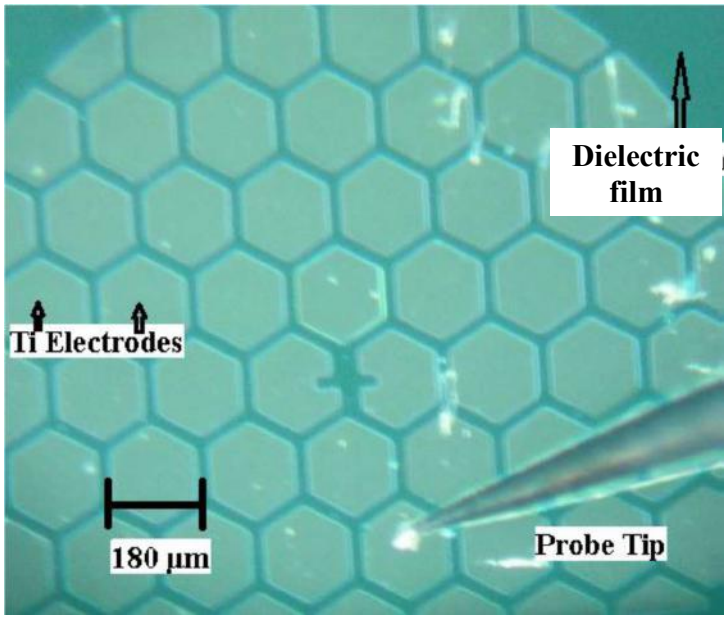

Figure 4. Optical micrograph of a typical MIS structure used in this work. Adapted from [4].

The grids were carefully placed on the sample surface and attached to the wafer surface using Kapton adhesive tape around the outer circumference of the grid. Because the electrodes needed for this work are relatively large, this technique allowed for sample fabrication without the complexity of photolithographic processes. Electrodes for the MIS structures were deposited through the TEM grid masks using e-beam evaporation at the Wisconsin Center for Applied Microelectronics (WCAM). Titanium was chosen as the electrode material for the structures used in this work. This Titanium layer is 300-nm thick.

A Signatone probe station with an optical microscope was used to make contact with the above-mentioned MIS structures for the leakage current measurements in this work. A photograph of the probe station is shown in Figure 5. This probe station consists of two movable micro positioners

with 20-µm diameter tungsten probe tips (Signatone SE-20T), and an X-Y wafer stage with a submicron resolution.

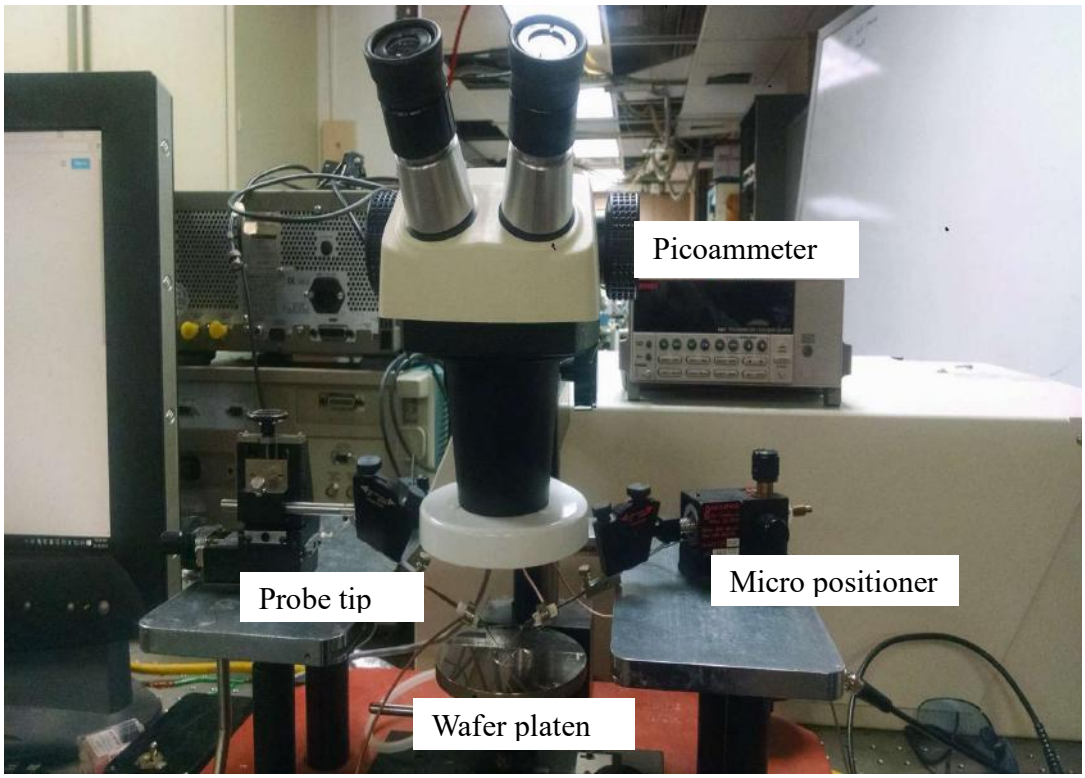

Figure 5. Photograph of the probe station used in this work. A Keithley 6487 picoammeter was connected to this probe station to provide a variable d.c source and also to measure the leakage current. A Labview program was used to control the measurements.

3.3.3 X-Ray Diffraction (XRD)

A Bruker D8 Discover x-ray diffraction system is a tool used to study the atomic structure of a crystal. Atoms cause the diffraction of x-rays and then the direction and magnitude of the diffracted x-rays are measured[5]. By measuring the angles and intensities of these diffracted beams, several properties, such as phase identification[6] of the material can be analyzed.

The Bragg Law[7] shown below describes the requirement to cause the diffraction of x-rays.

$$2d\sin\Theta = n\lambda \quad (6)$$

where d is the spacing of parallel atomic planes and Θ is the angle between the incident x-ray beam and the surface of the material. The geometric relation for the Bragg Law is shown in Figure 6.

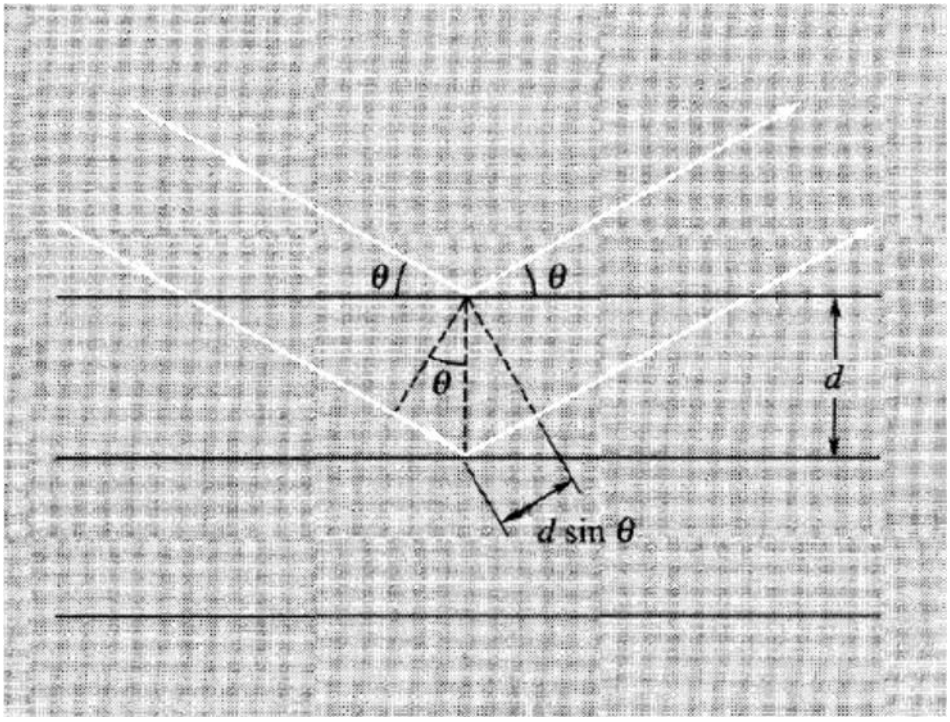

Figure 6. Drawing for the derivation of the Bragg equation. Adapted from [7].

An x-ray beam impinging on a crystal will be scattered in all directions by the atoms of the crystal. The scattered x-rays produce interference patterns based on the scales of the lattice. Thus, in some directions, an increased intensity is observed due to the constructive interference of the scattered x-rays. Constructive interference will be observed for x-rays that are reflected from the lattice

planes at given specular angles, if the path length difference between x-rays scattered from planes is an integer times the wavelength.

The diffraction can occur only for wavelengths $\lambda \leq 2d$. This is why we cannot use visible light because the wavelength of visible light is too large compared with the spacing of parallel atomic planes.

In this work, we use a two-dimensional diffractometer as shown in Figure 7.

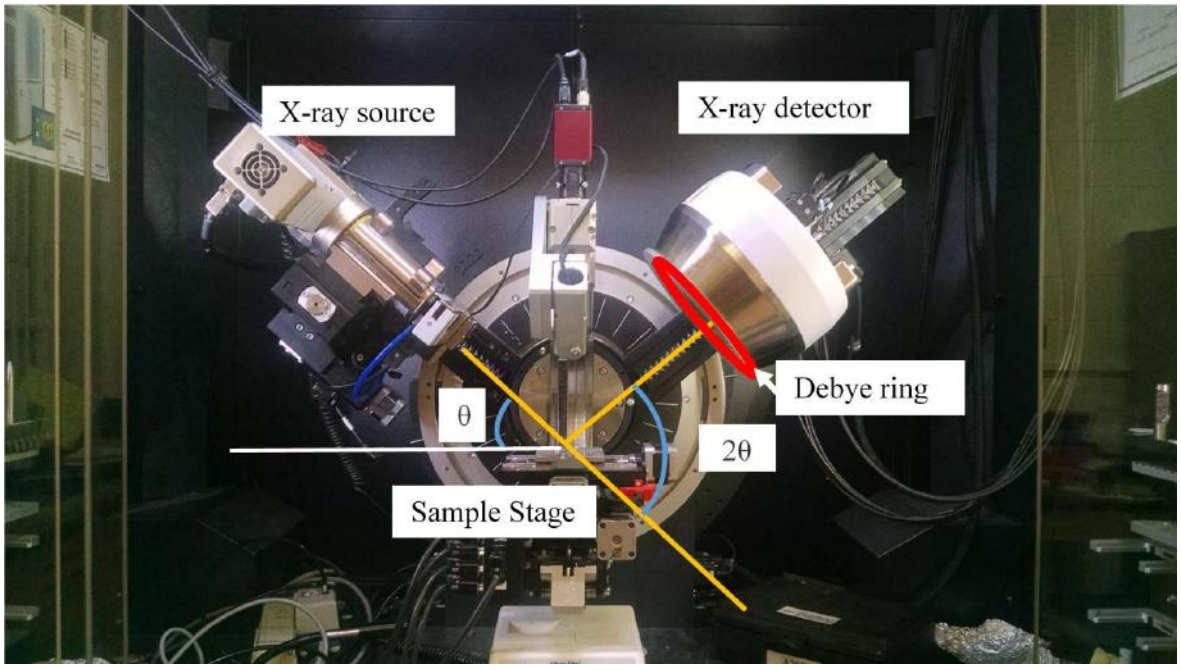

Figure 7. Two-dimensional XRD system.

It consist of an X-ray source (usually, an X-ray tube), a sample stage, a detector and a way to vary angle θ. The x-ray source is focused on the sample at angle θ while the detector opposite the source reads the intensity of the X-ray beam at angle 2θ away from the source path. The incident angle is then increased while the detector angle always remains at 2θ away from the source path. In addition, the diffraction data collected in this diffractometer is not confined to a single

plane.[8]Instead, the whole or a large portion of the diffraction rings (as called Debye rings[8]) can be measured simultaneously as shown in Figure 7.

Figure 8 shows the raw diffraction pattern collected with a 2D detector from corundum powder which is often used as a calibration for the XRD device and the HfO_2 film used in this work.

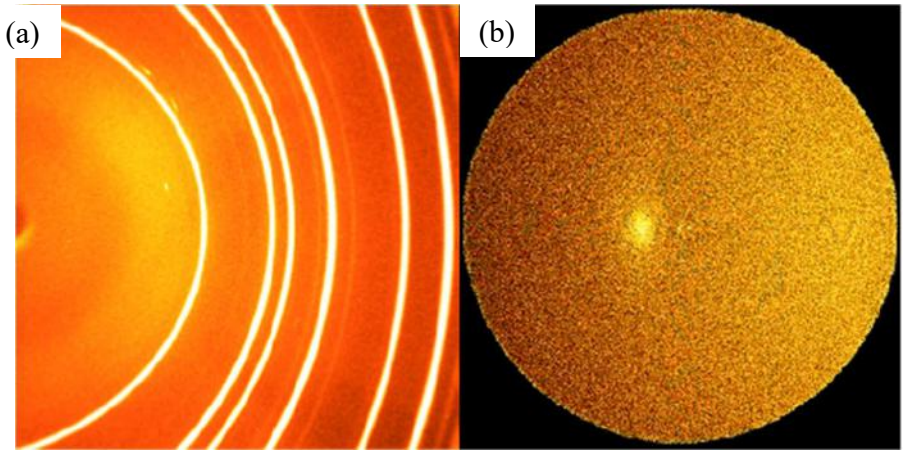

Figure 8. Two-dimension diffraction pattern for (a) corundum powder (Adapted from [8]) and (b) HfO_2 film used in this work.

The 2D diffraction pattern contains much information, such as phase identification, percent crystallinity, particle size, shape and texture.[9] In this work, we focus on the phase identification[6] of particular thin films. The two-dimensional diffraction pattern of any particular thin film is measured and the same method is also used to analysis the diffraction pattern for comparison purposes.[9]

3.4 Measurement of RRAM Properties

The device properties of both Type 1 and Type 2 RRAM cells were measured using two methods. They are: (1) I-V characteristics, (2) endurance testing.

3.4.1 I-V Characteristics

I-V characteristics of the RRAM devices were measured with an HP 4155B semiconductor parameter analyzer. The same probe station mentioned in the previous section was used in these measurements. The bottom electrode of the RRAM cell (Pt) was grounded and the signs of the positive/negative voltages mean positive/negative applied voltage across the device with respect to the bottom Pt electrode. In order to get the I-V characteristics of the RRAM device for the set and reset processes, an applied voltage was varied between 0 and 8 V and back from 8 to 0 V, followed by 0 to -8 V and then from -8V back to 0V. Each voltage step was 50 mV. The medium[10] measurement setting which represents the speed of the measurement was chosen in this work. The current compliance which limits current during the measurements is 100 μA.

3.4.2 Endurance testing

An endurance test was used to measure the number of pulsed-voltage cycles that can be applied to a RRAM device until it becomes unreliable.[11] The pulsed-voltage cycle was generated with a LabJack USB DAQ device and two function generators. The Labjack USB DAQ device is used to trigger the two function generators synchronously. The amplitude and waiting time are controlled by the two function generators. A common pulsed-voltage cycle used in endurance testing is shown in Figure 9. The resistances of the RRAM device were measured with an HP 4155B semiconductor parameter analyzer after every 500 pulsed-voltage cycles. A photograph of the experimental setup and circuit diagram is shown in Figure 10.

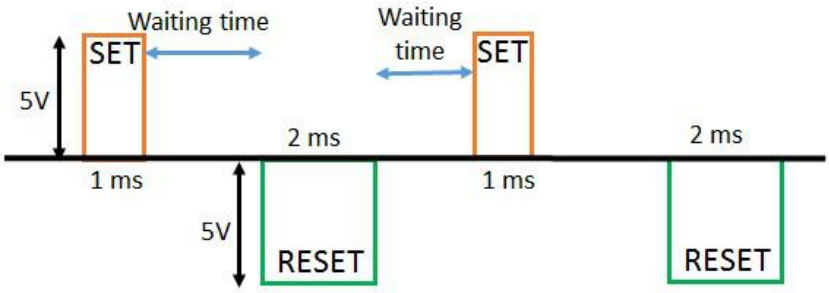

Figure 9. A positive voltage is need to achieve set prosess and a negative voltage for reset process. The amplitude and waiting time of the applied voltages need to vary because the variation of device properties.

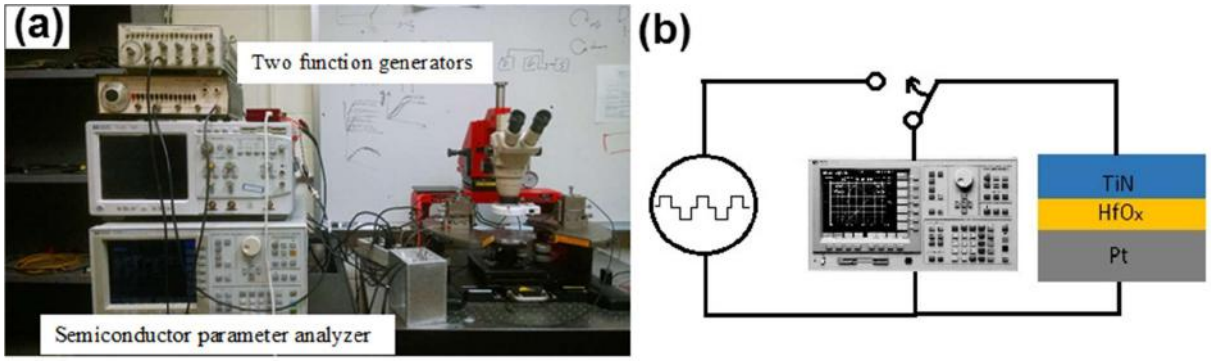

Figure 10. (a) Photograph of the experimental setup and (b) Circuit diagram for endurance test.

REFERENCES

[1] *Light water reactor*, WWW Document
(https://en.wikipedia.org/wiki/Light_water_reactor)

[2] *Particle accelerator*, WWW Document
(https://en.wikipedia.org/wiki/Particle_accelerator)

[3] L. J. F. Broer, "On the theory of paramagnetic relaxation," *Physica* **10** 810 (1943).

[4] Michael Thomas Nichols, Ph. D. thesis, University of Wisconsin-Madison, 2013.

[5] *X-ray crystallography*, WWW Document
((https://en.wikipedia.org/wiki/X-ray_crystallography)

[6] *Phase Identification,* WWW Document
(http://www.doitpoms.ac.uk/tlplib/xray-diffraction/phase_identification.php)

[7] Charles Kittel, Introduction to Solid state Physics, pp. 23-25.

[8] *COMPARISON BETWEEN CONVENTIONAL AND TWO-DIMENSIONAL XRD*, WWW Document
(http://www.icdd.com/resources/axa/vol46/v46_05.pdf)

[9] Charles Kittel, Introduction to Solid state Physics, pp. 23-43.

[10] *HP4155B-Agilent Technologies*, WWW Document)
(http://cp.literature.agilent.com/litweb/pdf/5968-6681E.pdf)

[11] Y. Y. Chen, R. Degraeve, S. Clima, B. Govoreanu, L. Goux, A. Fantini, G. S. Kar, G. Pourtois, G. Groeseneken, and D. J. Wouters ,"Understanding of the endurance failure in scaled HfO_2-based 1T1R RRAM through vacancy mobility degradation," *Tech. Dig. IEEE Int. Electron Devices Meeting*, 20 (2012).

Chapter 4 - Neutron-Induced Effects

In this Chapter, neutron-induced effects will be presented. Particular attention will be paid to two topics: (1) The effects of neutron irradiation on ultra-thin HfO_2 films. Several measurements were made including defect-state concentration, leakage current, and atomic structure (described in Section 4.1), and (2) The effects of neutron irradiation on two types of RRAM cells. Figure 1 shows the two types of RRAM cells. Type 2 HfO_x RRAM is different from the Type 1 RRAM in two aspects, (1) the thickness of the dielectric film and (2) the fabrication process for depositing the HfO_x within the RRAM.

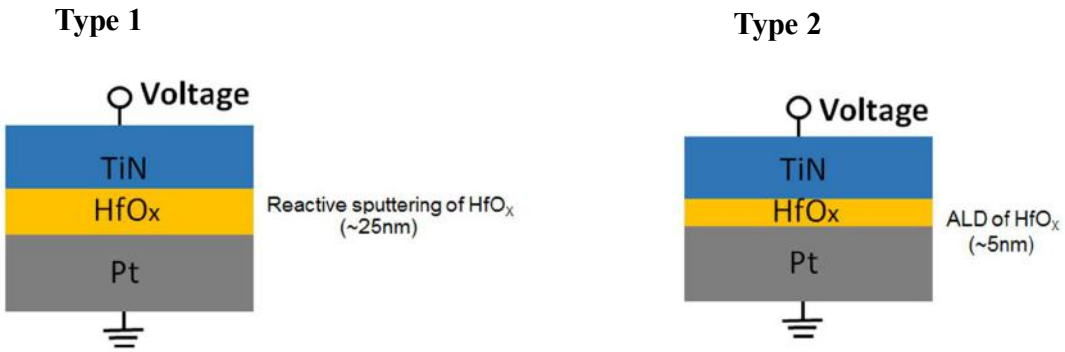

Figure 1. Schematic of Type 1 and Type 2 RRAM cells.

For the Type 1 HfO_x RRAM, as will be shown, neutrons do affect its performance (described in Section 4.2). In order to analyze their influence, several measurements were made, including the forming process, I-V characteristics, and endurance (described in Sections 4.2.1), sequential I-V characteristic measurements (described in Section 4.2.2), and the effects of RRAM cell area (described in Section 4.2.3). Based on these results, the Type 2 HfO_x RRAM is proposed (described in Section 4.3) to be more neutron resistant than the Type 1 RRAM.

4.1 Effects of neutron irradiation on ultra-thin HfO_2 blanket films

In this Section, blanket films of HfO_2 deposited on Si were irradiated with neutrons over a range of fluences at the University of Wisconsin Max Carbon Radiation-Science Center. Electron-spin resonance (ESR) was used to detect changes in the defect-state concentration. In addition, leakage currents in the HfO_2 films were measured to supplement the ESR data. X-ray diffraction was performed on the HfO_2 films to determine whether there were any changes in crystal structure after irradiation.

4.1.1 Electron-Spin Resonance Measurements

The HfO_2 blanket films were 20-nm thick room-temperature atomic-layer-deposited (ALD) on (100) Si. The resistivity of the silicon substrate was 4000 Ω-cm. This high resistivity was needed to obtain adequate ESR measurements.[1] The ESR analysis techniques were described in Section 3.3.1. Two sets of identical HfO_2 samples were irradiated with neutron fluences that are shown in Table I.

		Fluence	
Neutron Type	Thermal (<1eV)	Epithermal (>1eV,<1MeV)	Fast (>1MeV)
Set 1	1.33×10^{14} neutrons/cm^2	3.84×10^{12} neutrons/cm^2	1.76×10^{13} neutrons/cm^2
Set 2	1.33×10^{15} neutrons/cm^2	3.84×10^{13} neutrons/cm^2	1.76×10^{14} neutrons/cm^2

Table I. Neutron-fluence levels used for irradiation on the two sets of blanket films.

The ESR signals are shown in Figure 2, they are represented by black lines and can be decomposed into three defect states. The three defect state are Pb0, Pb1 and E'. These are the most common defects for HfO_2 film deposited on the Si substrate as described in Section 2.3.1.

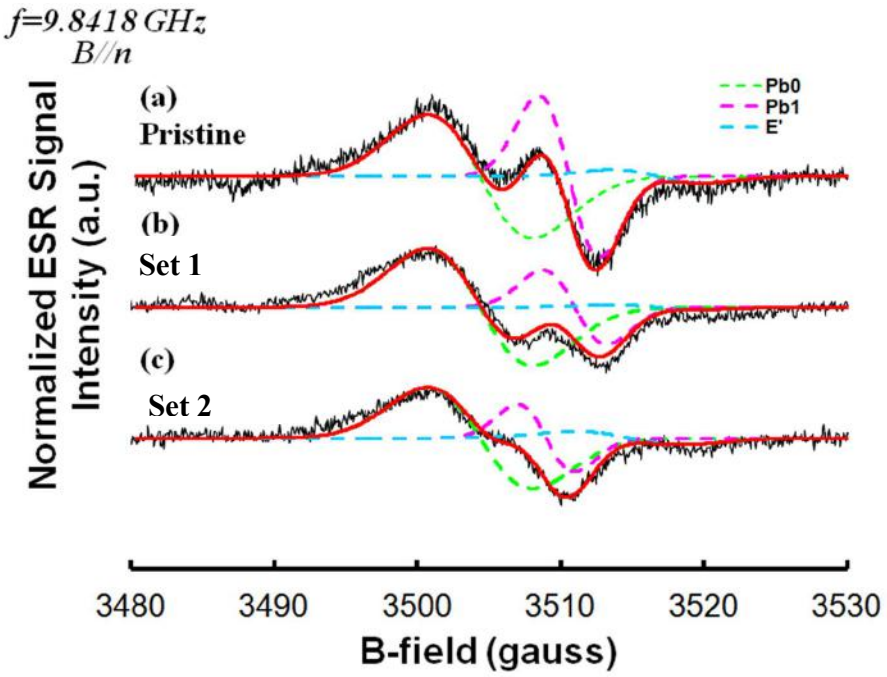

Figure 2. ESR signals and defect-state fitting curves for (a) pristine sample, (b) neutron-irradiated sample (set 1), and (c) neutron-irradiated sample (set 2). The two sets are described in Table I.

Figure 3 shows that the concentrations of the Pb0 and Pb1 states decrease after neutron irradiation. However the E' concentration, which is the oxygen-vacancy defect, first decreases when fluence increases, but it is followed by a bounce-back upwards in the sample at the highest radiation fluence.

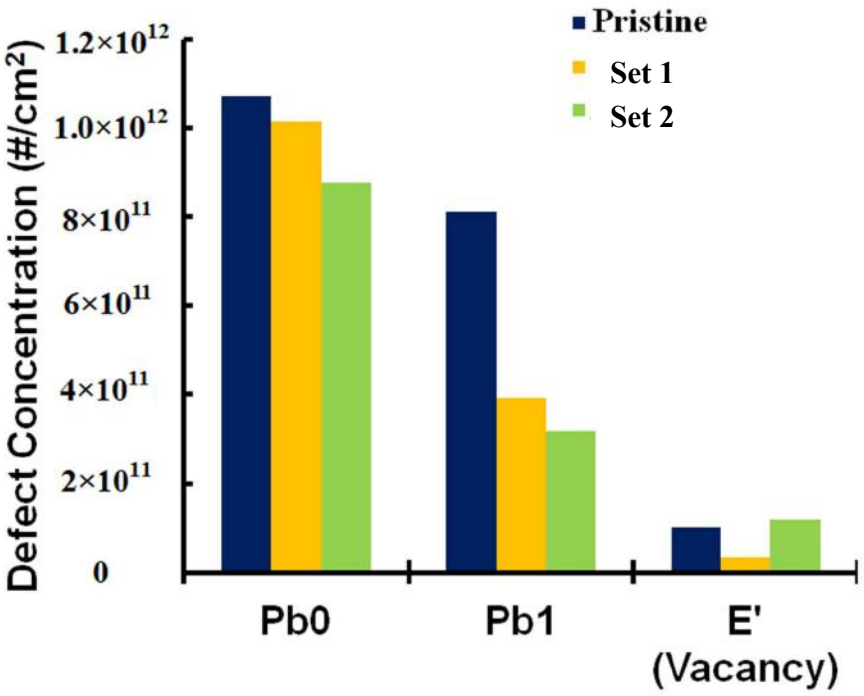

Figure 3. Absolute values of the defect-state concentrations. Sets 1& 2 are described in Table I.

There is a large body of literature that discusses the interaction between neutrons and semiconductor materials.[2,3,4] There is a consensus that neutrons displace atoms in the materials and cause emission of alpha particles, gamma rays or other particles along with the recoil of a daughter nucleus, each of which may cause ionization.[2] The cross sections for these reactions decrease rapidly with increasing neutron energy and generally follow a $1/E$ dependence. Since the HfO_2 in this work was irradiated in a light-water-moderated nuclear reactor where a continuous neutron spectrum is present including thermal, epithermal and fast (>1 MeV) neutrons, it is very likely that displaced atoms and electron-hole pairs were generated during irradiation. The generated electrons can then anneal the generated and existing Pb and E' states. Hence, the number of defect states decreases first. However, as the neutron fluence increases, an increasing number

of oxygen atoms are knocked out of the lattice structure, which leads to the formation of a greater number of oxygen vacancies.

4.1.2 Leakage-Current Measurements

In previous studies of high-k gate materials, the leakage currents through HfO_2 films were usually attributed to Poole-Frenkel emission.[5] The Poole-Frenkel mechanism generates conduction through defect states.[6] Thus, it is likely that leakage currents in HfO_2 film will be influenced by neutron radiation.

The leakage currents of the pristine sample and samples irradiated with three different neutron fluences are shown in Figure 4. It is clear that the leakage current decreases when the neutron fluence increases.

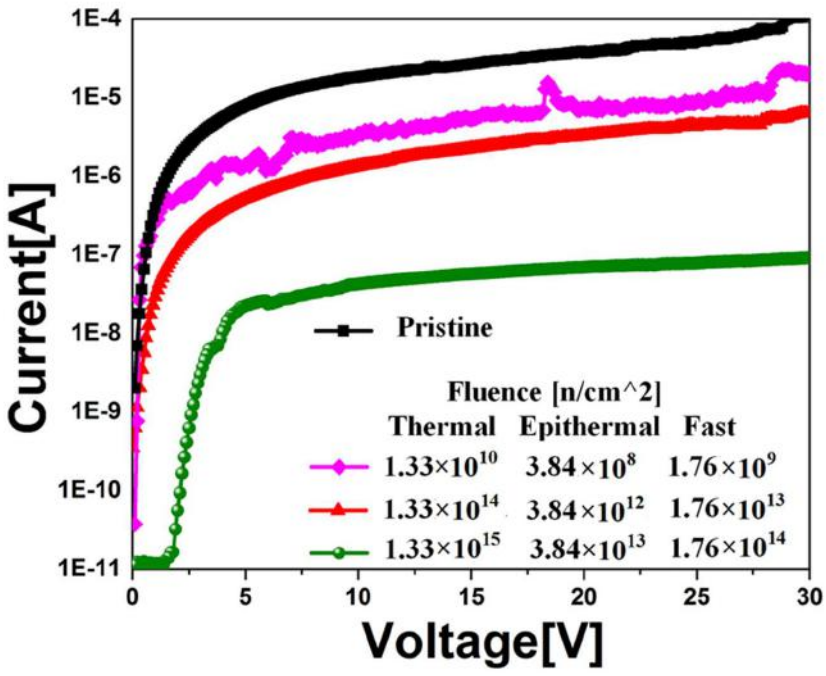

Figure 4. I-V characteristics of pristine and neutron-irradiated HfO_2.

It is noted that in this experiment, although the E' state concentration decreases and then increases at high neutron fluence, this defect has a negligible effect on the leakage current since the number of E' states is very small compared with the number of Pb-type states. The concentration of Pb-types always decrease when fluence increase.

Thus, the decrease in leakage current is believed to be due to the decrease in the number of Pb-type defect states, as was also shown in the ESR measurements. For pristine samples, the Pb-type defect states that are very near the Si/HfO_2 interface reduce the potential barrier at the surface of HfO_2, which enhances Poole-Frenkel conduction.[7] However, after neutron irradiation, the number of Pb-type defect states decreases, with a concomitant reduction in leakage current.

4.1.3 X ray diffraction measurements

Local atomic structures of HfO_2 films are changed as a result of neutron irradiation.[8] In order to gain more insight into the modification, x-ray diffraction (XRD) was performed on control and neutron-irradiated HfO_2 films. These results are shown in Figure 5. This shows that the pristine and irradiated films display polycrystalline monoclinic structure grains. [9] The increase in intensity of the peak ($2\Theta = 28.6°$) indicates that the HfO_2 film becomes more crystalline after neutron irradiation. Other work has reported[8,10,11] that tetragonal and cubic grains appear after neutron irradiation of as-deposited HfO_2 films with monoclinic structure.

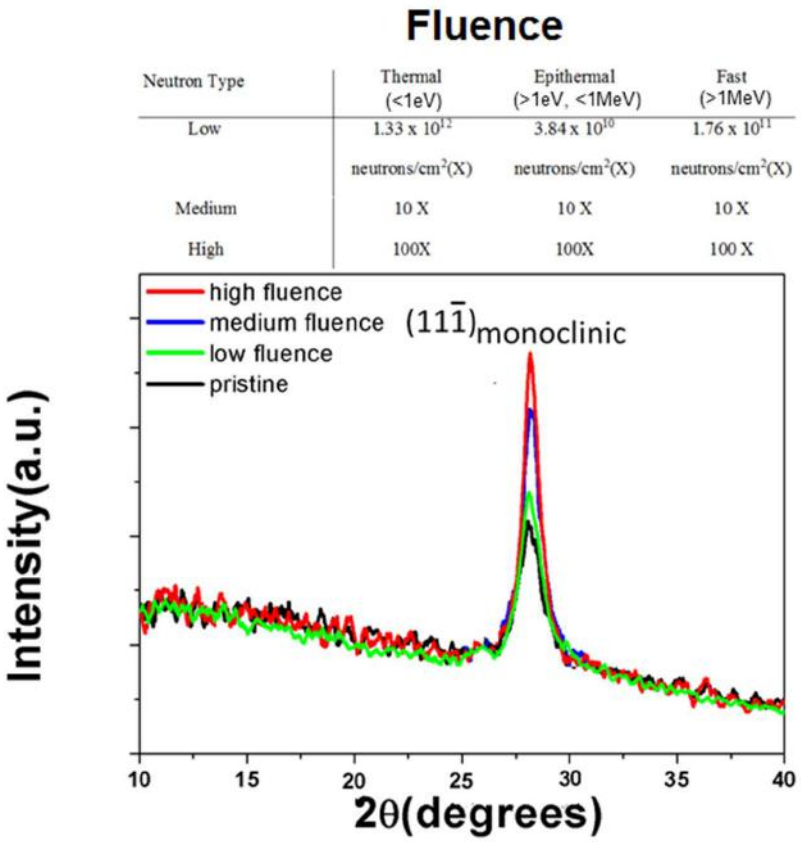

Figure 5. X-ray diffraction patterns of selected HfO_2 films grown on Si substrates.

4.2 Effects of neutron irradiation on Type 1 HfO_x RRAM

Here, Type 1 HfO_x RRAM cells shown in Figure 6 were irradiated with neutrons under three different fluences. The neutron fluences are shown in Table II

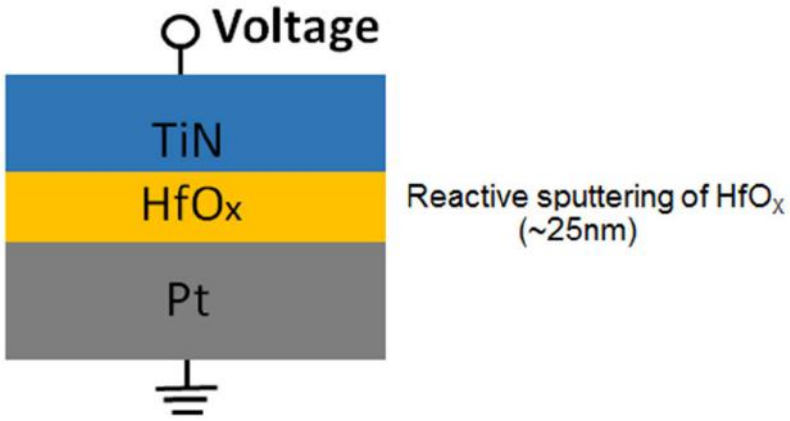

Figure 6. Schematic of Type 1 RRAM cell. HfO_x (~25 nm thick) was deposited with reactive sputtering. The bottom electrode (Pt) was grounded and voltage was applied to the top electrode (TiN) in all the measurements. Thus, positive/negative bias means applying positive/negative voltage to the TiN electrode.

Neutron Type	Thermal (<1eV)	Epithermal (>1eV, <1MeV)	Fast (>1MeV)
Low	1.33×10^{12} neutrons/cm^2(X)	3.84×10^{10} neutrons/cm^2(X)	1.76×10^{11} neutrons/cm^2(X)
Medium	10 X	10 X	10 X
High	100X	100X	100 X

Table II. Three neutron fluences for Type 1 RRAM.

The investigation of the effects of neutrons on the Type 1 HfO_x RRAM are separated into three parts: (1) Type 1 RRAM performance as a function of neutron radiation fluence, (2) Sequential I-V characteristic measurements on irradiated Type 1 RRAM, and (3) Area effects on irradiated Type 1 RRAM. All the investigations use the same HfO_x Type 1 RRAM cells as shown in Figure 6. The neutron fluence levels and energies are shown in Table II.

4.2.1 Type 1 RRAM performance as a function of neutron radiation fluence

In this section, neutron effects on the Type 1 RRAM, particularly on the forming rate, the forming voltage, the resistances of the high resistance state (HRS), the shift in set voltage, and endurance are analyzed.

4.2.1.1 Forming Rate and Forming Process

According to a review paper published by Wong, [12] a forming process is needed for fresh RRAM because the number of intrinsic defects in the metal oxide is typically small. To produce the forming process, a d.c. voltage that is higher than the set/reset voltage is applied across the metal oxide. The forming voltage results in oxygen ions leaving the lattice of the metal oxide and moving toward the anode. The localized deficiency of oxygen leads to the formation of a conduction path[12] that makes RRAM end up in the low-resistance state (LRS)[13]. However, in the case of neutron irradiation, RRAM cells can be formed under irradiation.

Figure 7 shows the forming rate of irradiated RRAM cells as a function of neutron fluence. The forming rate is the ratio of the number of Type 1 RRAM cells that changed their resistance under neutron irradiation to the total number of Type 1 RRAM cells. For each fluence, 50 Type 1 RRAM cells were irradiated and measured. It is clear that the forming rate increases nearly linearly when neutron fluence increases.

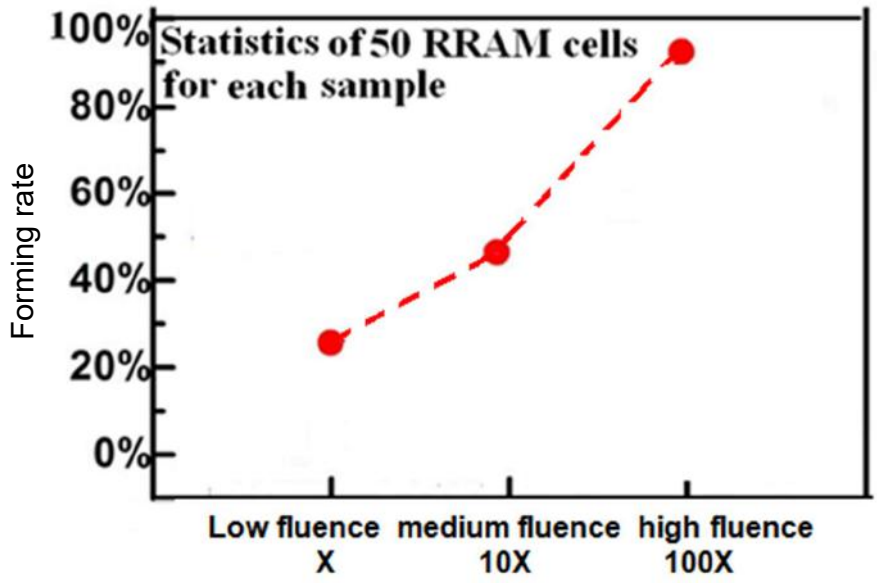

Figure 7. Forming rate as a function of neutron fluence (averaged over 50 Type 1 RRAM cells).

It can be seen in Figure 7 that 90 % of Type 1 RRAM cells are formed after being irradiated with high neutron fluence. This indicates that neutrons create oxygen vacancies in the HfO_x.[5] These oxygen vacancies form a conduction path which makes the RRAM end up in the LRS.[12]

Next, the forming voltages for *unformed* neutron-irradiated Type 1 RRAM cells were measured. These results are shown in Figure 8. For those unformed neutron-irradiated Type 1 RRAM cells, smaller forming voltages were needed.

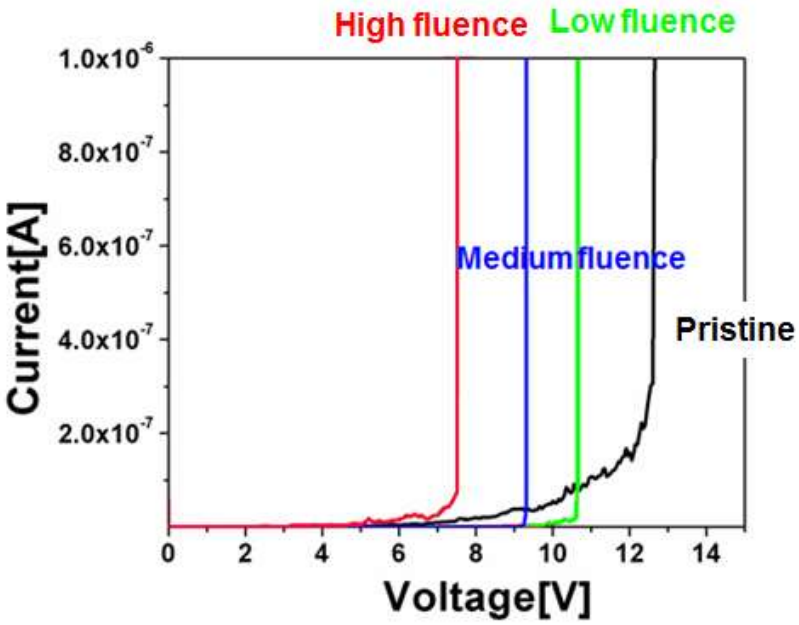

Figure 8. Forming voltages of Type 1 RRAM cells under three irradiation conditions.

From both the forming rate and the forming voltage measurements, it is apparent that *either* neutrons or the forming voltage can result in the formation of a conduction path.

4.2.1.2 I-V Characteristics

The I-V characteristics of formed Type 1 RRAM cells are shown in Figure 9. The annealing effect appears as an increase in the resistance of the HRS.

In addition, the neutron-induced effects on Type 1 HfO_x RRAM devices agrees with our observations for blanket films,[14] which showed that neutrons anneal the HfO_2 films. This resulted in measurements that showed increasing fluence decreases the leakage current. In addition, this type of radiation-induced anneal in RRAM devices was also observed by Zhang[15] where gamma rays annealed TaO_x-based RRAM.

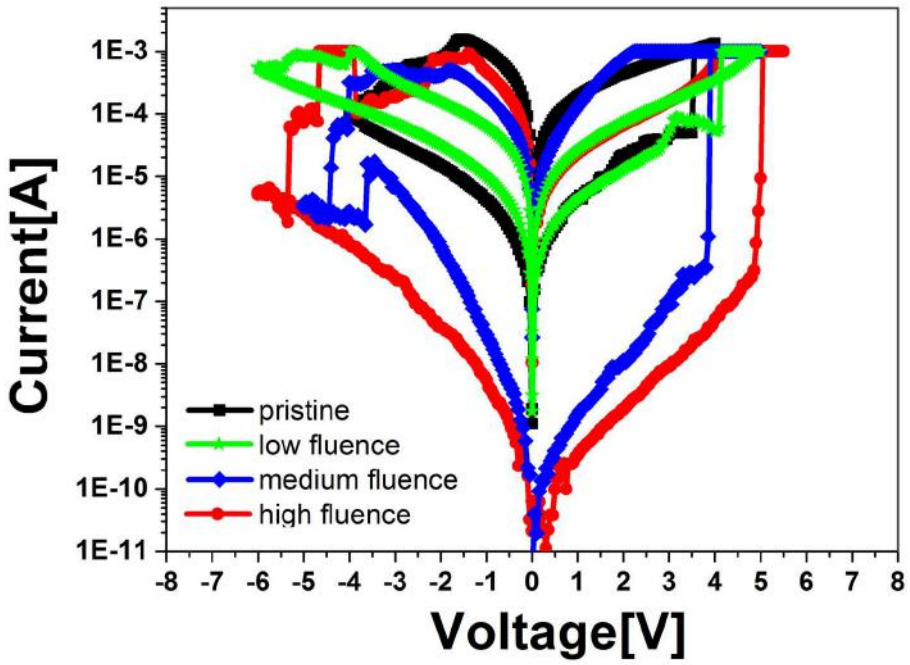

Figure 9. I-V characteristics of pristine Type 1 RRAM cells and Type 1 RRAM cells irradiated by three different neutron fluences.

Set voltages were also measured for the Type 1 RRAM cells after neutron irradiation. Figure 10 shows the shifts of the set voltage. For pristine Type 1 RRAM, the set voltages was approximately 3.5V. Note that the variation of the set voltages from cell to cell is very small. For Type 1 RRAM cells exposed to high neutron fluence, at least 5V were needed to achieve the set process. Such shifting in set voltages might lead to a malfunction of Type 1 RRAM cells because after irradiation they do not appear to switch at fixed pulse voltages.

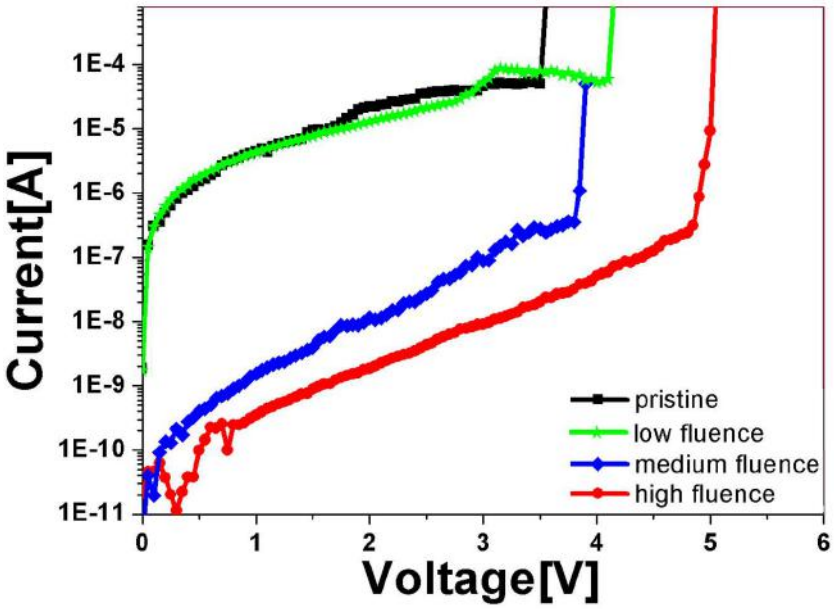

Figure 10. Set voltages of Type 1 RRAM cells irradiated with three different neutron fluences.

4.2.1.3 Endurance

Next, the endurance of pristine Type 1 RRAM that was exposed to high-neutron-fluence was measured. The experimental setup and circuit diagram are shown in Chapter 3 (3.4.2). The endurance test measures the number of pulsed-voltage cycles that can be applied to a Type 1 RRAM until it becomes unreliable.[16] Figure 11 shows a pulse cycle applied to Type 1 RRAM during the endurance test. Figure 12 is the result of this endurance test. A Type 1 RRAM is said to fail the endurance test when its resistance is stuck in the HRS state.

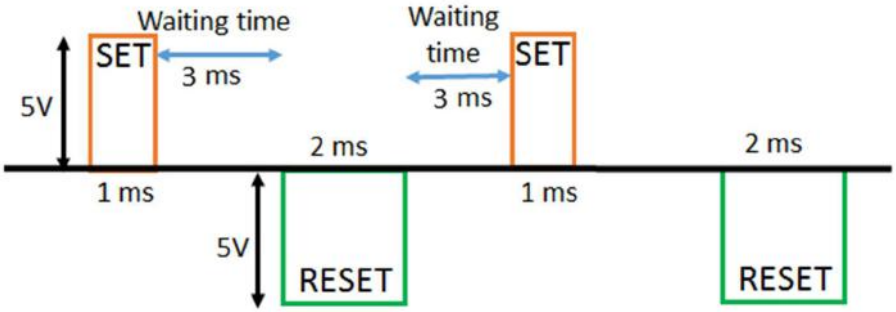

Figure 11. A pulse cycle applied to Type 1 RRAM during the endurance test. For every cycle, t_{cycle} = SET pulse width + RESET pulse width + waiting times = 9ms.

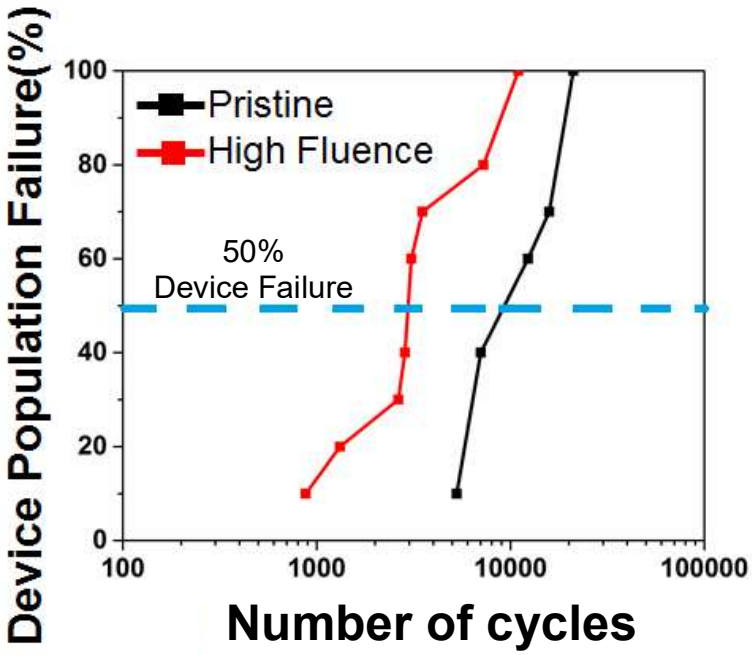

Figure 12. Pulse endurance cycles for pristine and high-neutron-fluence irradiated Type 1 RRAM.

This is also called the SET failure mode.[16] From Figure 12, it is obvious that the endurance of Type 1 RRAM cells degrades after neutron irradiation.

Summary of Section 4.2.1

From these observations, some conclusions about neutron-induced effects can be drawn. First, defects created by neutrons can create a conduction path in the HfO_x. The conduction path created by the neutrons is very similar to the conduction path created by the applied voltage during the forming process. Second, neutrons also anneal the HfO_x film used in Type 1 RRAM. This results in a higher high-resistance state (HRS) value. Third, shift in values of the set voltage can be seen on the I-V characteristic of neutron-irradiated Type 1 RRAM. In other words, it is more difficult to produce the set process when the Type 1 RRAM has been irradiated. In addition, a consistent result from the endurance test is observed. That is, the irradiated Type 1 RRAM lasts for fewer switching cycles and finally stop with their resistance remaining in the HRS state. The increase in set voltage and degradation in endurance of irradiated Type 1 RRAM is believed to be the result of atomic-structure changes in HfO_x caused by neutron irradiation.

4.2.2 Sequential I-V characteristic measurements on irradiated Type 1 RRAM

In the previous section, the performance of Type 1 RRAM cells over a range of neutron fluences was discussed. In this section, sequential I-V characteristic measurements of Type 1 RRAM cells at specific neutron fluences are presented. We want to examine whether these neutron-induced effects are permanent or recoverable after several switching cycles. The neutron fluences used here are the highest level listed in Table II.

Figure 13 shows the sequential I-V characteristic measurements of Type 1 RRAM cells after high neutron fluence. All Type 1 RRAM cells begin in the LRS state from neutron irradiation. All I-V characteristics start from the most negative voltage resulting in a switch from LRS to HRS. After this step, a positive voltage was applied to the Type 1 RRAM to switch from HRS to LRS. The

combined set of negative and positive voltage swings generates a switching cycle. For all measurements shown in this section, the black lines are the first switching cycle, followed by red, blue, green, and pink cycles, respectively.

Measurements for several irradiated Type 1 RRAM cells are shown because of the variation between Type 1 RRAM cells. It is seen that the I-V characteristics vary from cycle to cycle for all Type 1 RRAM cells. Finally, the I-V characteristics of the irradiated Type 1 RRAM cells are similar to the pristine Type 1 RRAM. Therefore, it can be assumed that the influence of high-neutron-fluence irradiation does not last after several switching cycles.

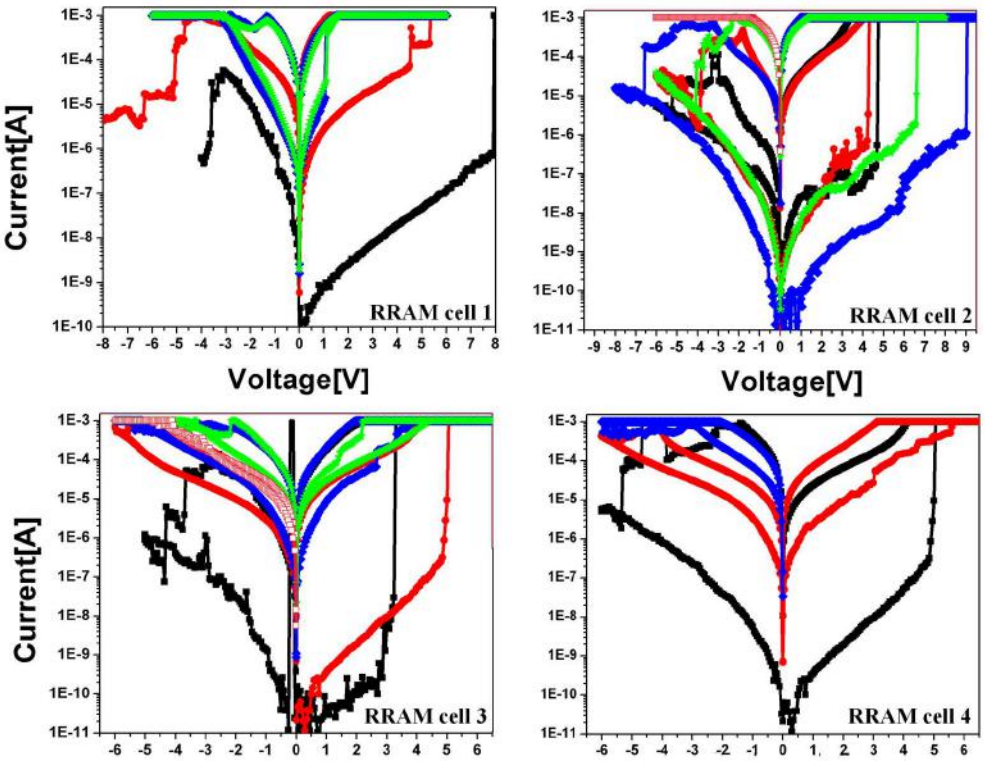

Figure 13. I-V characteristics of Type 1 RRAM cells irradiated with high neutron fluence. The black lines are the first switching cycle, followed by red, blue, green, and pink lines.

4.2.3 Area effects on irradiated Type 1 RRAM

In this section, Type 1 RRAM cells with different areas were exposed to the same neutron fluence. This was done so that the neutron-induced effects, especially the production of oxygen vacancies (discussed in Section 4.2.1) can be analyzed. The oxygen vacancies construct a conduction path and affect the LRS resistance. If the resistance of the LRS is dependent on the exposed area, then oxygen vacancies generated by neutrons would be a function of the exposed area. Figure 14 shows the resistance of the LRS at several Type 1 RRAM-cell sizes.

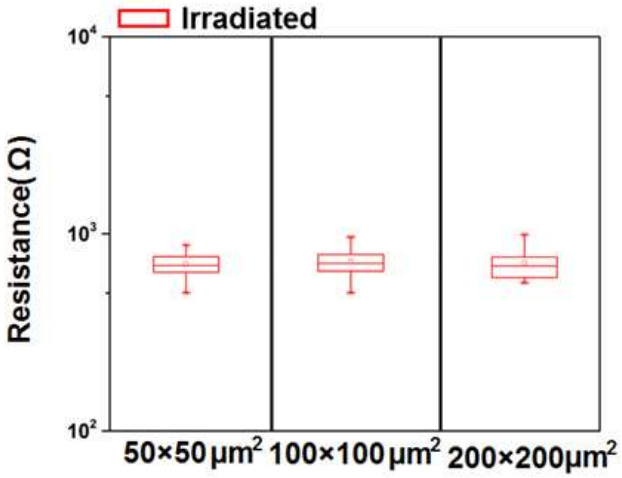

Figure 14. Resistance of LRS (Type 1 RRAM cells irradiated by high neutron fluence) with different areas.

It is obvious that the resistance of LRS exhibited very little dependence on area. This implies that although even more oxygen vacancies are generated in a large-size Type 1 RRAM, only a small portion of them form the oxygen conduction path. Thus, other oxygen vacancies generated in the

large-size Type 1 RRAM may deviate from the conduction path(s), resulting in little change in the resistance of the LRS.

4.3 Effects of neutron irradiation on Type 2 HfO_x RRAM

In this section, Type 2 RRAM was subjected to the same irradiation as Type 1 RRAM. Figure 15 shows the schematic of the Type 2 RRAM cell.

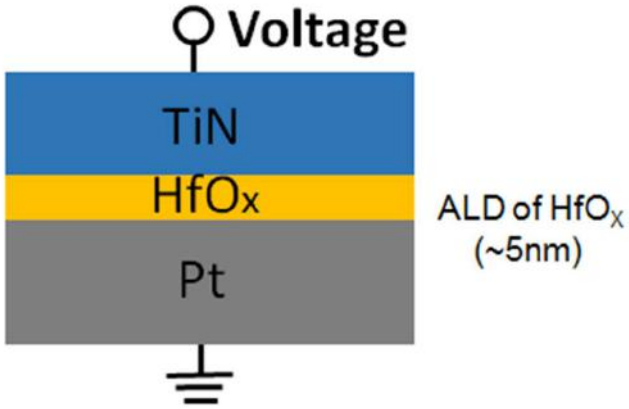

Figure 15. Schematic of the Type 2 RRAM cell. As mentioned previously, this RRAM cell is modified from Type 1 in the following two ways: (1) reduction in the thickness of the HfO_x, and (2) use of Atomic-Layer Deposition to deposit the HfO_x layer (~5 nm).

These two modifications (reduction of the thickness and changing the fabrication process of HfO_x) were made for several reasons. First, in the past, the influence of gamma rays on TaO_x RRAM devices with different thicknesses was investigated.[15] The results indicated that RRAM with thinner oxides have less degradation in both the HRS and LRS resistance after gamma-ray irradiation.[15] Based on this clue, we propose that a thinner oxide RRAM is one possible way to increase the radiation hardness.

Second, some variations were seen in the reliability test for Type 1 RRAM cells. We expect that the quality of the HfO_x film will become better and hypothesize that a good-quality film might have a higher degree of radiation hardness. It has been known that the quality of ALD films is better compared to sputter-deposited films.[17] Hence, the fabrication process of the HfO_x film was changed from sputter deposition to ALD.

The Type 2 RRAM cells (shown in Figure 15) were exposed to very high neutron fluence as shown below.

	Thermal	Epithermal	Fast
.	(<1eV)	(>1eV, <1MeV)	(>1MeV)
	1.33×10^{14}	3.84×10^{12}	1.76×10^{13} (neutrons/cm^2)

4.3.1. Type 2 RRAM performance under neutron irradiation

The forming rate, the forming voltage, the resistances of the high resistance state (HRS), the shift in set voltage of the irradiated Type 2 RRAM cells were measured. No Type 2 RRAM cells were found to be formed and end up in the LRS after high-neutron-fluence irradiation

Figure 16 shows the forming voltage for pre-irradiated and post-irradiated Type 2 RRAM cells. All forming voltages were approximately 7 V. There was no significant change in them after neutron irradiation. Figure 17 shows the I-V characteristics for pre-irradiated and post-irradiated Type 2RRAM cells.

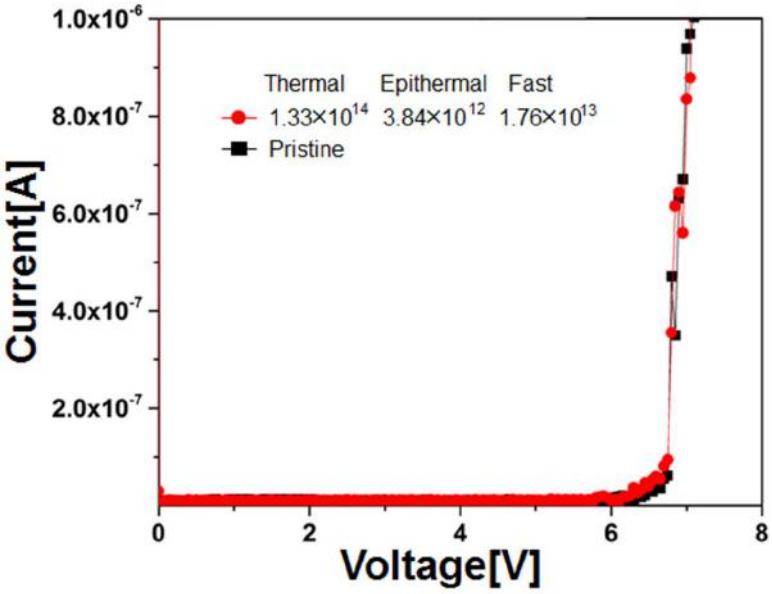

Figure 16. Forming voltages of pristine and post-irradiated Type 2 RRAM cells

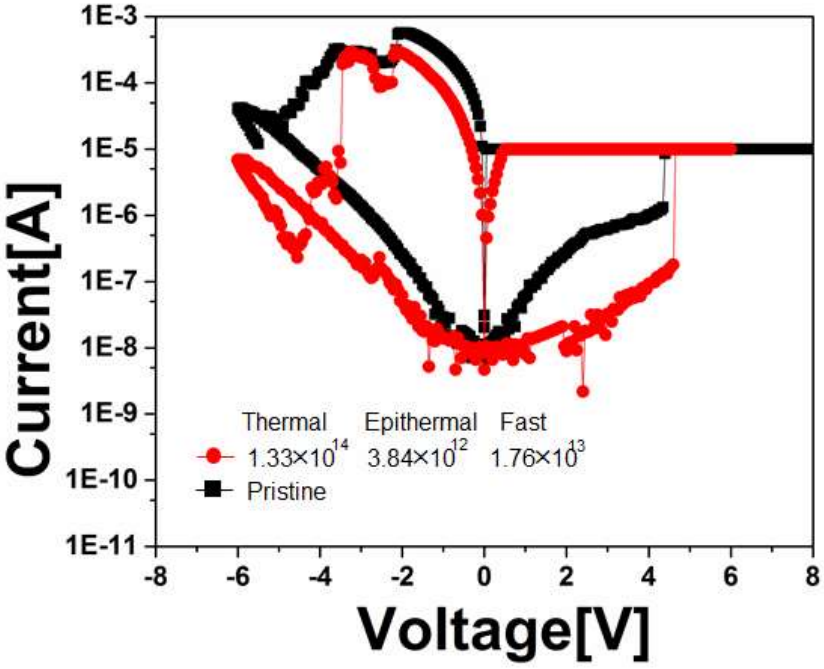

Figure 17. I-V characteristics of pri-irradiated and post-irradiated Type 2 RRAM cells

There is no significant influence generated by neutrons in the resistance of HRS, and set voltages.

4.3.2 Sequential I-V characteristic measurements on irradiated Type 2 RRAM

Figure 18 shows the sequential I-V characteristic measurements on the irradiated Type 2 RRAM cells. The black lines are the first switching cycle, followed by red, blue, pink, and yellow lines. There is no significant variation from cycle to cycle.

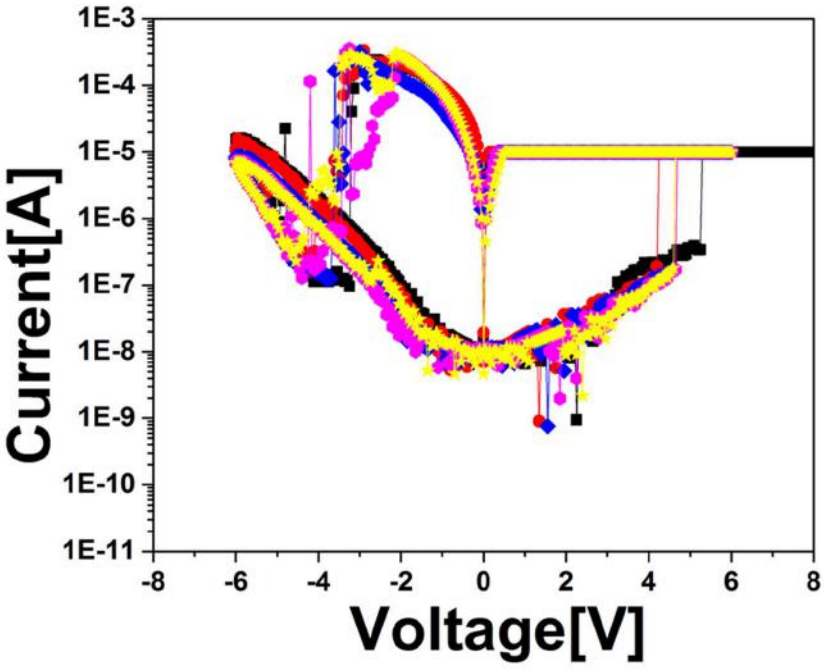

Figure 18. Sequential I-V characteristic measurements on the irradiated Type 2 RRAM cells.

Summary of Section 4.3

Type 2 RRAM is not formed under high-fluence neutron irradiation, and no significant changes in the forming voltage and I-V characteristics appeared after neutron irradiation. For the sequential I-V characteristic measurements, no obvious variation is observed. Hence, the Type 2 RRAM can

be considered to be resistant to high neutron fluence. Since all the Type 2 RRAM cells had both the thickness and the fabrication method of the cell changed, it will be helpful to speculate on which of these two effects are dominant. It is very likely that both the changes in thickness and fabrication are very important since these two modifications can cut down on the number of defects. In addition, it was found that the forming voltage is linearly dependent on the thickness of the oxide film[18]. Obvious, it is not desirable to have a high forming voltage in practical applications. Thus this points to the use of a thinner oxide within a RRAM cell.[18]

4.4 Summary

Neutrons displace atoms and produce electron-hole pairs. This effects result in decreases the Pb-type defects levels in ultra-thin HfO_2 films. Thus, we may say that lower doses of neutrons "anneal" the sample. However, when the neutron radiation dose increases, more and more neutrons collide with oxygen atoms and cause them to leave the lattice or to transmute into different atoms. This step then causes the number of E' states to increase. These defect states are related to the electron transport in HfO_2. Therefore, the leakage currents in HfO_2 can change as the defect concentrations are changed.

These neutron-induced effects are also observed at Type 1 RRAM. Many Type 1 RRAM cells can be formed by neutron irradiation and end up in the LRS. This effect indicates that neutrons create conduction paths in the HfO_x, which makes the Type 1 RRAM at the LRS. On the other hand, unformed neutron-irradiated Type 1 RRAM only needs a lower voltages to form. In addition, the resistance of the HRS increased and anneal effects are observed on the HfO_x film within the Type 1 RRAM. The shift in values of the set voltage can be seen on the I-V characteristic of the neutron-irradiated Type 1 RRAM. Degradation of endurance is also observed on irradiated Type 1 RRAM.

This is believed to be the result of atomic-structure changes in HfO_x film caused by neutron irradiation. From the sequential I-V characteristic measurements of high-neutron fluence-irradiated Type 1 RRAM cells, the influence from neutron irradiation does not last after several switching cycles.

No effect of cell area on irradiated Type 1 RRAM cells was seen. This infers that some oxygen vacancies generated in large size Type 1 RRAM cells are dislocated from the conduction path.

Based on all the measurements about how neutrons affect Type 1 RRAM, the Type 2 RRAM design was fabricated and shown to be resistant to high neutron fluence.

REFERENCES

[1] M. Tabib-Azar, D. Akinwande, G. E. Ponchak, and S. R. LeClair, "Evanescent microwave probeson high-resistivity silicon and its application in characterization of semiconductors," *Rev. Sci. Instrum.* **70**, 3083 (1999).

[2] R. C. Baumann, "Radiation-induced soft errors in advanced semiconductor technologies," *IEEE Trans. Device Mater. Rel.* **5**, 305 (2005).

[3] J. R. Srour, C. J. Marshall, and Paul W. Marshall, "Review of displacement damage effects in silicon devices," *IEEE Trans. Nucl. Sci.* **50**, 653 (2003)

[4] M. Hillman, and E. Shikata, "Cross sections of some reactions of hafnium isotopes with 14.5-MeV neutrons," *J. Inorg. Nucl. Chem.* **31**, 909 (1969).

[5] S. Yu, X. Guan, and H.-S. Philip Wong, "Conduction mechanism of TiN/HfO_x/Pt resistive switching memory: A trap-assisted-tunneling model," *Appl. Phys. Lett.* **99**, 063507 (2011).

[6] W. S. Lau, "An Extended Unified Schottky-Poole-Frenkel Theory to Explain the Current-Voltage Characteristics of Thin Film Metal-Insulator-Metal Capacitors with Examples for Various High-k Dielectric Materials," *ECS J. Solid State Sci. Technol.* **1** N139 (2012).

[7] J. T. Ryan and P. M. Lenahan. "Interfacial layer defects and instabilities in HfO_2 MOS structures," *IEEE Int. Rel. Phys. Symp. Proc.,*665(2008).

[8] *HIGH NEUTRON DOSE IRRADIATION OF DIELECTRIC MIRRORS*, WWW Document (http://web.ornl.gov/sci/physical_sciences_directorate/mst/fusionreactor/pdf/Vol.55/5.2%20Leonard.pdf)

[9] N. V. Nguyen, A. V. Davydov and D. C. Horowitz, "Sub-bandgap defect states in polycrystalline hafnium oxide and their suppression by admixture of silicon," *Appl. Phys. Lett.* **87**, 192903 (2005).

[10] A. Benyagoub, "Swift heavy ion induced crystalline-to-crystalline phase transition in zirconia and hafnia: a comparative study," *Nucl. Instrum. Methods Phys. Res., Sect. B* **218**, 451 (2004).

[11] I. O. Usov, J. A. Valdez, J. Won, M. Hawley, D. J. Devlin, R. M. Dickerson, B. P. Uberuaga, Y.Q. Wang, C. J. Olson Reichhardt, G. D. Jarvinen, and K. E. Sickafus, "Irradiation effects in an HfO_2/MgO/HfO_2 tri-layer structure induced by 10MeV Au ion," *Nucl. Instrum. Methods Phys. Res., Sect. B* **267**, 1918 (2009).

[12] H.-S. Philip Wong, H-Y Lee, S. Yu, Y. S. Chen, Y. Wu, P-S Chen, B. Lee, F. T. Chen, and M-J Tsai, "Metal–oxide RRAM," *Proc. IEEE* **100**, 1951 (2012).

[13] I. H. Inoue, S. Yasuda, H. Akinaga and H. Takagi," Nonpolar resistance switching of metal/binary-transition-metal oxides/metal sandwiches: Homogeneous/inhomogeneous transition of current distribution," *Phys. Rev. B* **77**, 035105 (2008).

[14] K.-W. Hsu, H. Ren, R. J. Agasie, S. Bian, Y. Nishi and J. L. Shohet, "Effects of neutron irradiation of ultra-thin HfO_2 films," *Appl. Phys. Lett.* **104**, 032910 (2014).

[15] L. Zhang, R. Huang, D. Gao, P. Yue, P. Tang, F. Tan, Y. Cai and Y. Wang, "Total ionizing dose (TID) effects on-based resistance change memory," *IEEE Trans. Electron Devices* **58**, 2800 (2011).

[16] Y. Y. Chen, R. Degraeve, S. Clima, B. Govoreanu, L. Goux, A. Fantini, G. S. Kar, G. Pourtois, G. Groeseneken, D. J. Wouters ,"Understanding of the endurance failure in scaled HfO_2-based 1T1R RRAM through vacancy mobility degradation," *Tech. Dig. IEEE Int. Electron Devices Meeting*, 20 (2012).

[17] James D. Plummer, Michael D. Deal and Peter B. Griffin, Silicon VLSI Technology: Fundamentals, Practice and Modeling, pp. 539-554

[18] H. Y. Lee, P. S. Chen, T.Y. Wu, Y. S. Chen, C. C. Wang, P. J. Tzeng, C. H. Lin, F. Chen, C.H. Lien and M,-J. Tsai," Low power and high speed bipolar switching with a thin reactive Ti buffer layer in robust HfO_2 based RRAM," *Tech. Dig. IEEE Int. Electron Devices Meeting*, 1 (2008).

Chapter 5 - Proton-Induced Effects

In this Chapter, proton-induced effects will be presented. This discussion will be separated into three parts: (1) Transport of Ions in Matter (TRIM) code calculation for protons interacting with materials (described in Section 5.1), (2) The effects of proton irradiation on ultra-thin HfO_2 blanket films. Several measurements were made including defect-state concentration, leakage current, and atomic structure (described in Section 5.2), and (3) The effects of proton irradiation on the two types of RRAM cells. For the Type 1 HfO_x RRAM, protons affect its performance (described in Section 5.3). In order to analyze the influence of protons, several measurements were made including the forming process, the I-V characteristics, endurance (described in Section 5.3.1), and sequential I-V characteristic measurements (described in Section 5.3.2). Based on these results, the Type 2 HfO_x RRAM is proposed (described in Section 5.4) to be more proton resistant than the Type 1 RRAM.

5.1 TRIM Code calculations for protons interacting with material

There is a large body of literature discussing the interactions between protons and materials.[1,2] The interaction of protons with materials results in two major effects: production of electron-hole pairs (ionization)[3] and physical displacement of atoms (displacement).[4] Those interactions that result in electronic excitation or ionization of atoms are referred to as the ionization/excitation process. For protons, this process can be direct ionization/excitation since protons are charged particles. In the displacement process, the energy imparted by the incident particles results in atoms leaving their original lattice structure. Once defects are formed by the displacement process, these defects will attempt to reorder to form more stable configurations. Defect reordering is often called

annealing.[5] In addition, this phenomenon is enhanced by free charged particles generated during the ionization process.[6]

TRIM (the Transport of Ions in Matter) code calculations[7] were performed to determine the proton interactions. The code calculates the ion distribution and a number of kinetic phenomena associated with ion energy loss, such as displacement and ionization. In this work, we focus on several MeV protons since cosmic ray protons are in this energy range.[8] However, protons lose energy when they pass through matter.[9] Thus, lower-energy protons are also investigated.

Figure 1-3 shows the results of the TRIM calculations. The HfO_2 film thickness was set to be 20-nm and the Si substrate thickness was set to be 200 nm, which is the same as the blanket films. The proton energies were set to several MeV, several hundred keV and several tens of keV, since we are interested in protons with different energies. The simulation results include qualitative discussions on ionization and displacement and the tracks of the protons within the material.

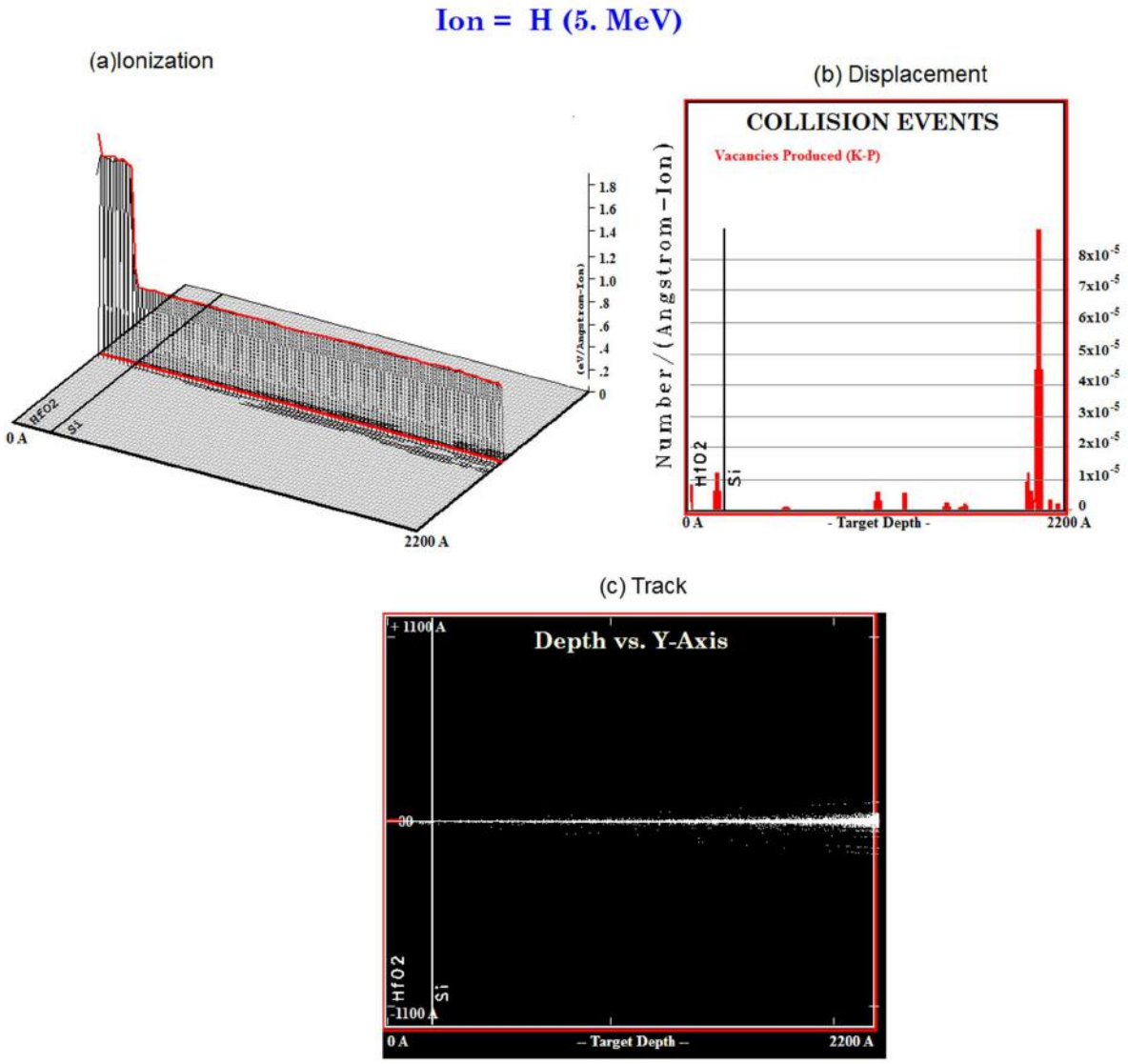

Figure 1. TRIM Code calculation of 5 MeV protons passing through a HfO_2 thin film and Si substrate: (a) Ionization, (b) Displacement, and (c) Tracks of protons.

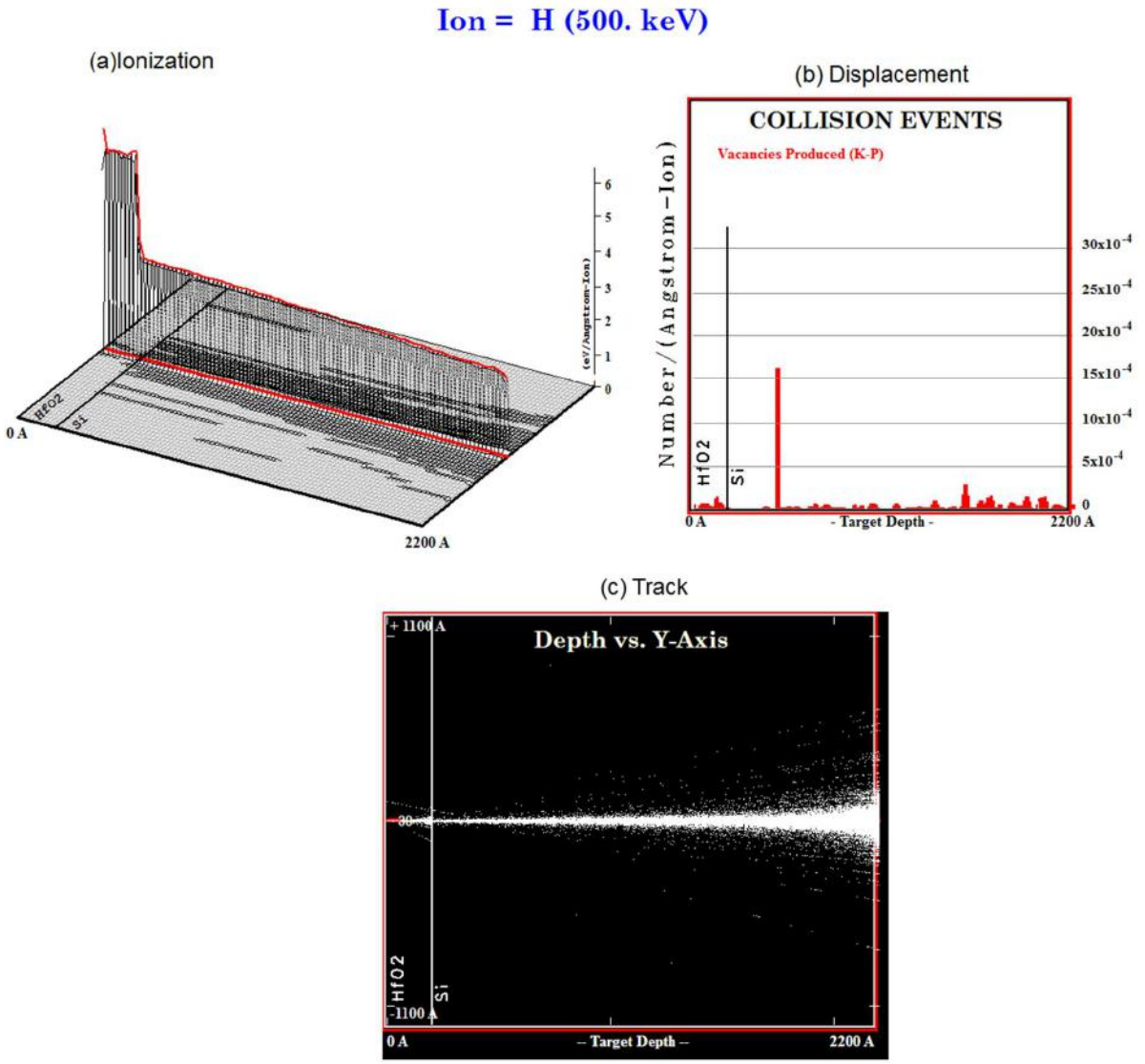

Figure 2. TRIM Code calculation of 500 keV protons passing through a HfO_2 thin film and Si substrate: (a) Ionization process, (b) Displacement process, and (c) Tracks of protons.

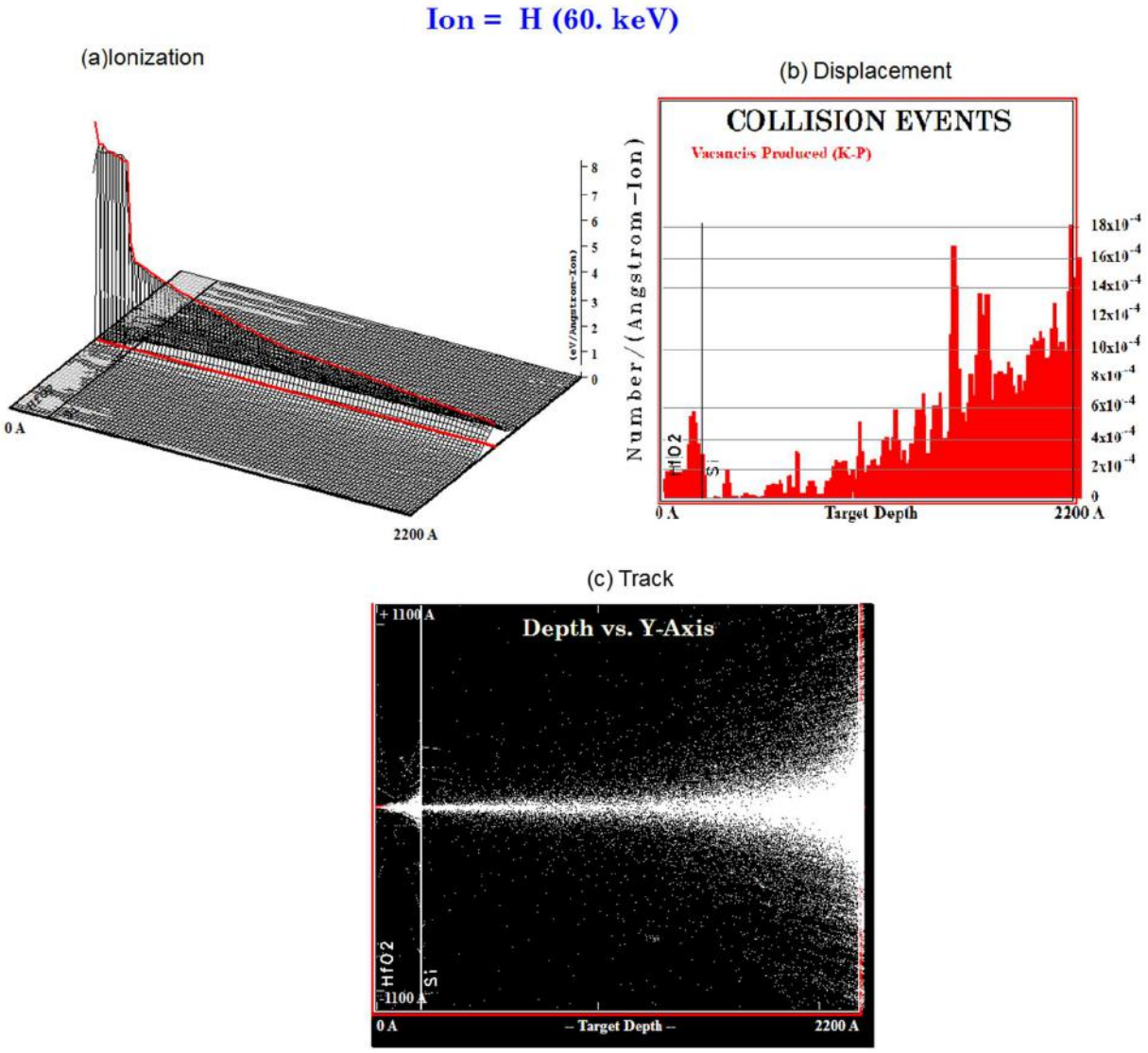

Figure 3. TRIM Code calculations for 60 keV protons passing through a HfO_2 thin film and Si substrate: (a) Ionization process, (b) Displacement process, and (c) Track of protons.

It can be seen in Figure 1 that only a very few 5 MeV protons interact with atoms and cause very little displacement. A similar simulation result was shown by Timotijevic *et al.*[2] That is, high-energy protons were shown to pass through SiO_2, AlN, Al_2O_3 and polycarbonate thin films, but did not produce much atomic displacement. It can be seen in Figure 3 that there is more atomic displacement and less transmission probability when proton energy is decreased to 60 keV.

The main goal here is to investigate proton-induced effects on blanket films and RRAM. As described earlier, the energies of the protons vary because of energy losses caused by collisions with matter. In this work, only 5 MeV and 60 keV protons were chosen for irradiation. This was done based on the TRIM-code results.

5.2 Effects of neutron irradiation on ultra-thin HfO_2 blanket films

In this Section, blanket films of HfO_2 deposited on Si were irradiated with protons with two fluences. These are: (1) ~2×10^{14} protons/cm^2 and (2) ~2×10^{15} protons/cm^2. The proton energies were set to 5 MeV and 60 keV for both fluences.

Electron-spin resonance (ESR) was used to detect changes in the defect-state concentration. In addition, the leakage currents of pristine and irradiated HfO_2 films were also measured. X-ray diffraction was also used to detect changes in crystal structure for these proton-irradiated samples. These are the same diagnostic measurements used for the neutron-irradiated HfO_2 films.

5.2.1 Electron-Spin Resonance Measurements

In this work the HfO_2 films were 20-nm thick room-temperature atomic-layer-deposited on (100) Si as was the case for the neutron-irradiated films. The resistivity of the silicon substrate was 4000 Ω cm. This resistivity was needed to obtain adequate ESR measurements.[10] The ESR analysis techniques were the same as those used for the neutron-irradiated HfO_2 films.

i) 5MeV protons

The measured and fit ESR data for the pristine and 5 MeV proton-irradiated samples are shown in Figure 4.

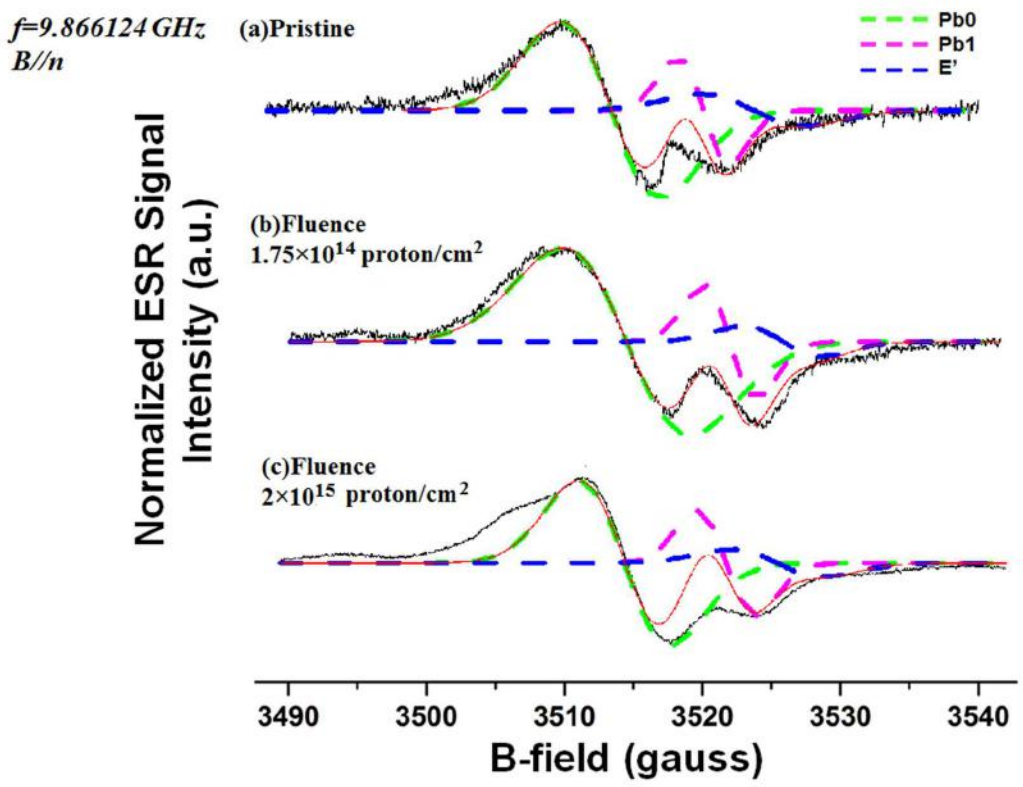

Figure 4. ESR signals and defect-state fitting curves for (a) Pristine sample, (b) 5MeV proton-irradiated sample (1.75×10^{14} protons/cm^2), and (c) 5MeV proton irradiated sample (2×10^{15}protons/cm^2).

The corresponding defect-state concentrations are shown in Figure 5.

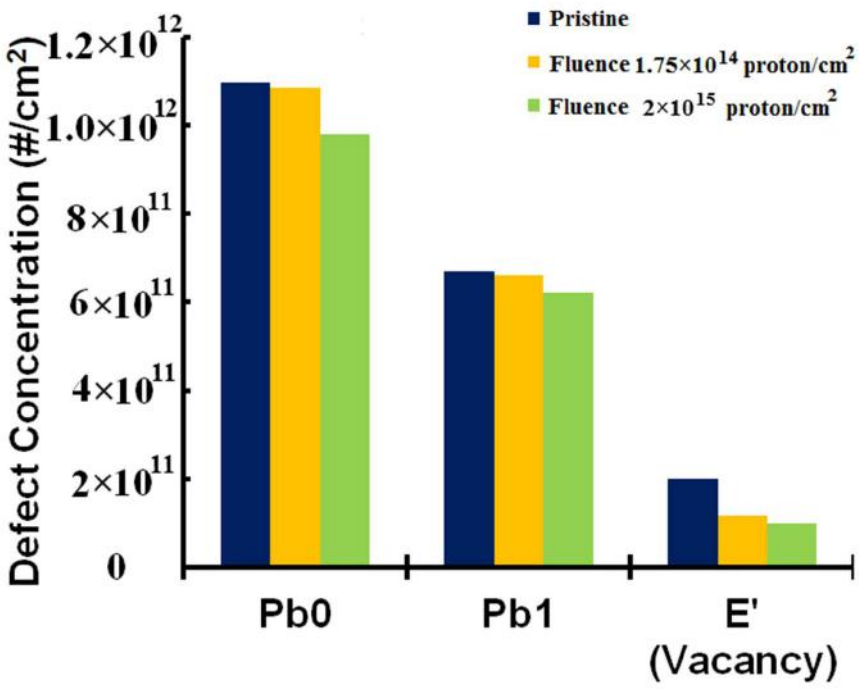

Figure 5. Absolute values of the defect-state concentrations.

Figure 5 shows that the concentrations of the Pb0 and Pb1 states change after proton irradiation. However, after considering experimental error, the results for 5 MeV protons cannot be regarded as a statistically significant change in concentration of any of these defects including Pb0, Pb1, and E' even after being exposed to a very high proton fluence. According to previous TRIM code calculations, very few effects of 5 MeV protons should be observed as is shown in the case here.

ii) 60keV protons

The measured and fit ESR data for the pristine and 60 keV protons irradiated samples are shown in Figure 6.

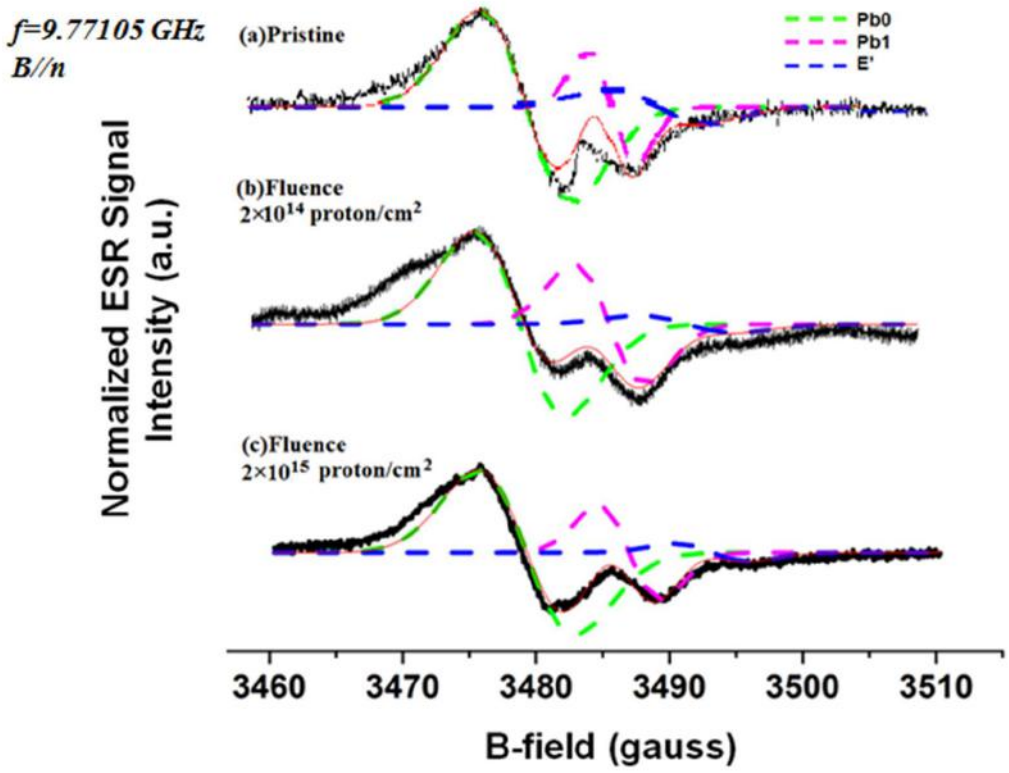

Figure 6. ESR signals and defect-state fitting curves for (a) Pristine sample, (b) 60 keV proton-irradiated samples (2×10^{14} protons/cm^2), and (c) 60 keV proton-irradiated samples (2×10^{15}protons/cm^2).

The corresponding defect-state concentrations are shown in Figure 7.

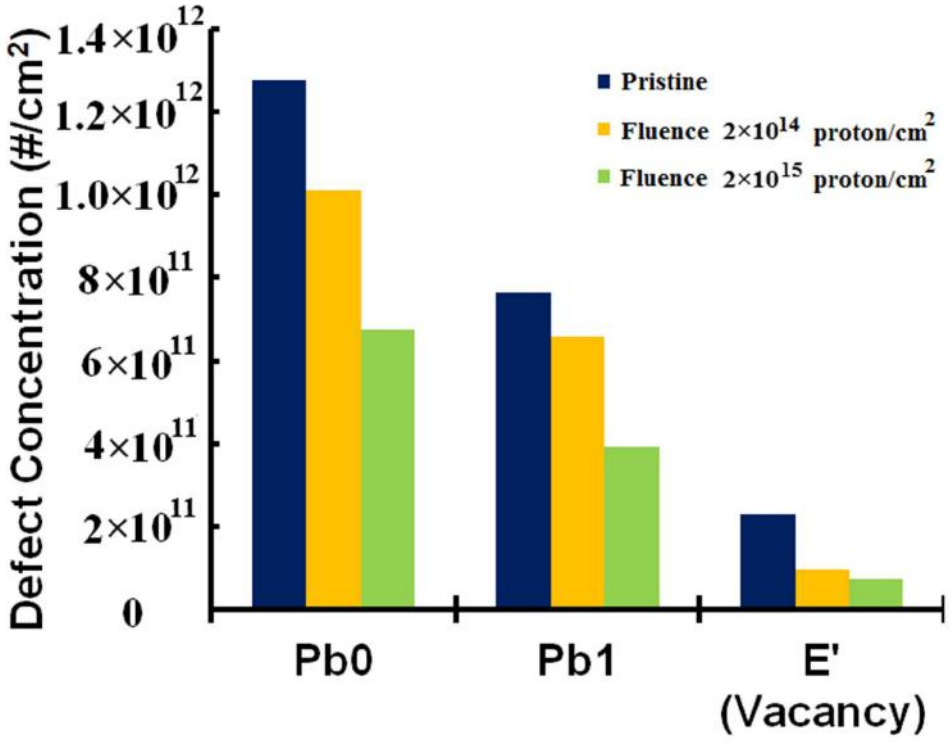

Figure 7. Absolute values of the defect-state concentrations.

Figure 7 shows that the concentrations of the Pb0, and Pb1 states decrease after proton irradiation. According to previous TRIM code calculations, there should be more displacement effects observed for 60 keV protons, which is the case here. The defect reordering enhanced by the charged particles generated by ionization (annealing) is also observable.[5]

5.2.2 Leakage-Current Measurements

Leakage currents through HfO_2 are usually attributed to Poole-Frenkel emission,[11] which generates conduction through defect states.[12] Therefore, the leakage currents after proton irradiation were also measured to determine whether this is consistent with the ESR measurements.

i) 5MeV protons

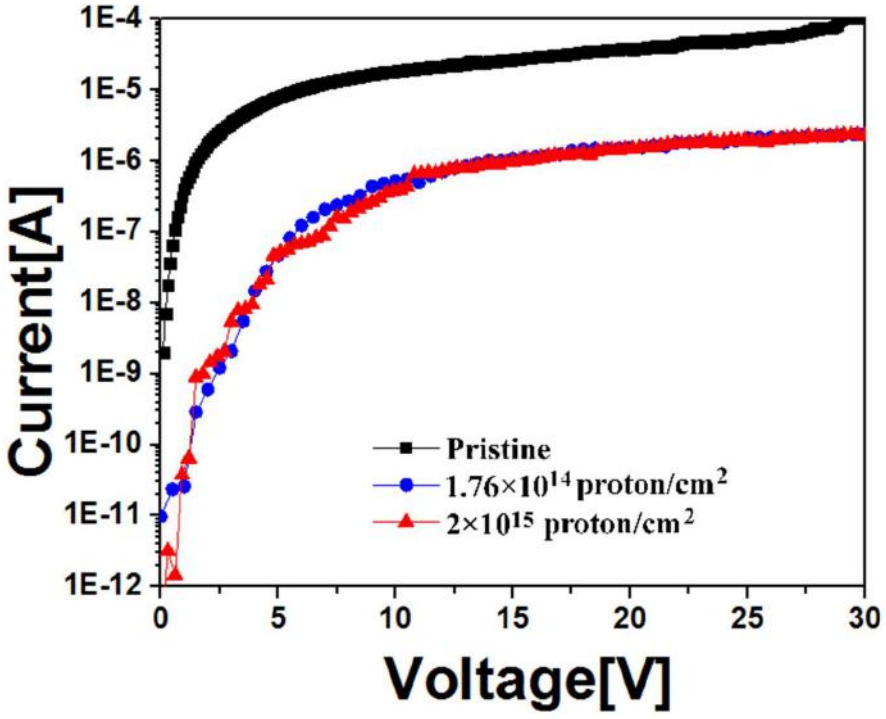

Figure 8. I-V characteristics of pristine and 5 MeV proton-irradiated HfO_2 films.

For 5 MeV proton irradiation, the changes in leakage currents (shown in Figure 8) are more obvious than the changes in defect-state concentration that were shown in Figure 5. Thus, we can conclude that there are still some observable annealing effects after exposure to 5 MeV protons.

ii) 60 keV protons

The annealing effect is observed in the 60 keV proton-irradiated samples as shown in Figure 9. This result is consistent with previous defect-state concentration measurements that were shown in Figure 7.

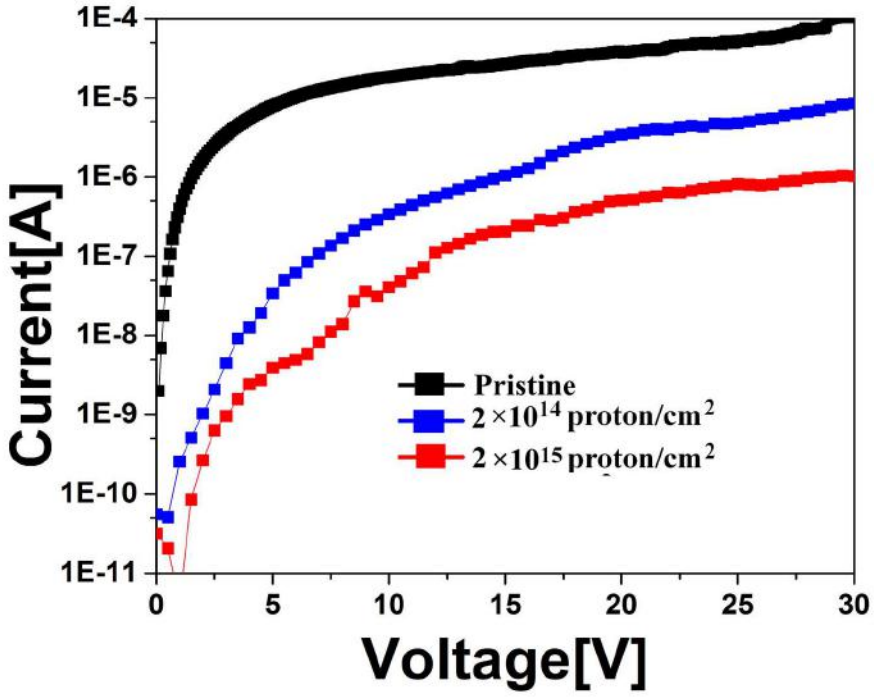

Figure 9. I-V characteristics of pristine and 60 keV proton irradiated HfO_2 films.

5.2.3 X-ray diffraction measurements

Local atomic structures of HfO_2 films can be changed as a result of proton irradiation.[13,14] In order to gain more insight into the modification, XRD was performed on a control and two proton-irradiated HfO_2 films.

i) 5MeV protons

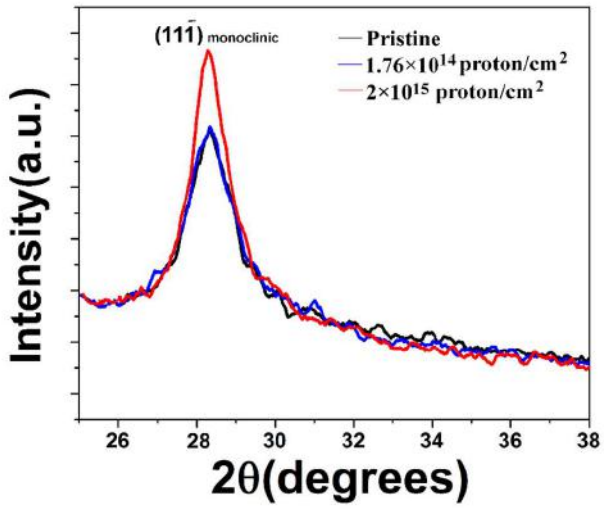

Figure 10. X-ray diffraction patterns of selected HfO_2 films grown on Si substrates.

ii) 60keV protons

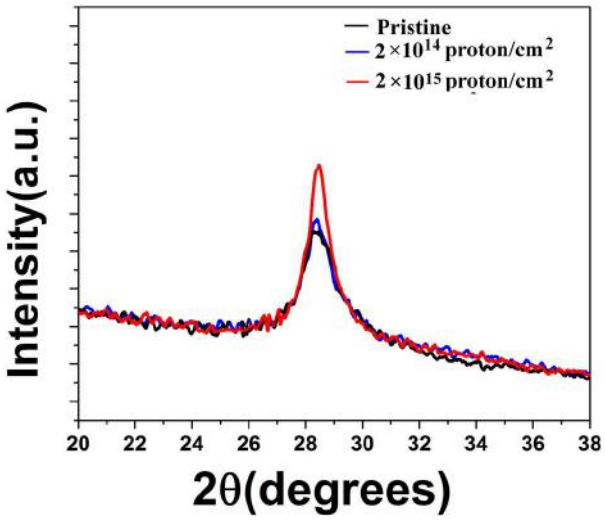

Figure 11. X-ray diffraction patterns of selected HfO_2 films grown on Si substrates.

It appears that both the pristine and irradiated films display polycrystalline monoclinic structure grains.[15] The increase in intensity of the peak ($2\Theta = 28.6°$) indicates that the HfO_2 films become more crystalline after both 5 MeV and 60 keV proton irradiation.

5.3 Effects of proton irradiation on Type 1 HfO_x RRAM

For reference, the schematic structure of the HfO_x-based Type 1 RRAM cell is shown again in Figure 12. HfO_x-based Type 1 RRAM cells were irradiated with 2 different proton levels: (1) ~2 × 10^{14} protons/cm^2 and (2) ~2 × 10^{15} protons/cm^2. The proton energies were again set to 5 MeV and 60 keV.

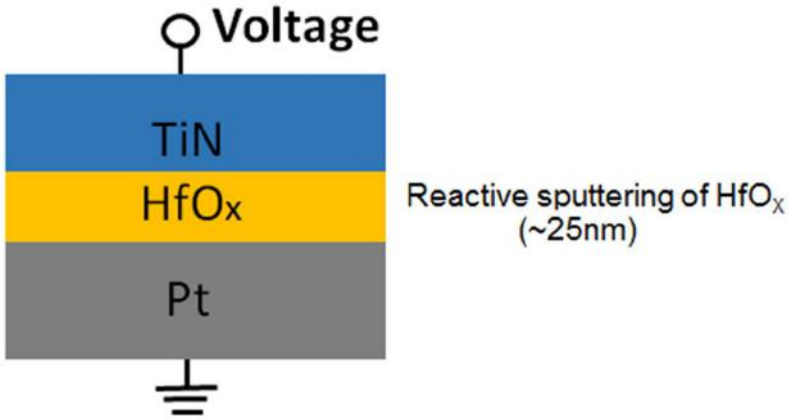

Figure 12. Schematic of Type 1 RRAM cell. The bottom electrode (Pt) was grounded and voltage was applied to the top electrode (TiN) in all the measurements. Thus, positive/negative bias means applying positive/negative voltage to the TiN electrode.

The investigation of the influence of protons on the Type 1 HfO_x RRAM can be separated into two parts: (1) Type 1 RRAM performance as a function of radiation fluence, and (2) Sequential I-V characteristic measurements on irradiated Type 1 RRAM. All the investigations use the same Type 1 HfO_x RRAM cells shown in Figure 12 as described previously.

5.3.1 Type 1 RRAM performance as a function of radiation fluence

In this section, proton effects, particularly on the forming rate, the forming voltage, the resistances of the high resistance state (HRS), the shift in set voltage and endurance are analyzed.

5.3.1.1 Forming Rate and Forming Voltage

For each fluence, 50 Type 1 RRAM cells before forming were irradiated. The forming rate and the forming voltages of these irradiated Type 1 RRAM cells were measured.

i) 5MeV protons

No Type 1 RRAM cells were formed so as to end up in the low-resistance state (LRS) even after being exposed to high 5 MeV proton fluence ($2.79 \times 10^{15} cm^{-2}$). The forming voltages for the irradiated Type 1 RRAM cells after irradiation are shown in Figure 13.

No differences were found in the forming voltages for both pristine and all Type 1 RRAM cells under 5 MeV proton irradiation. From these results, it is likely that 5 MeV protons do not affect the formation of a conduction path in the metal-oxide film.

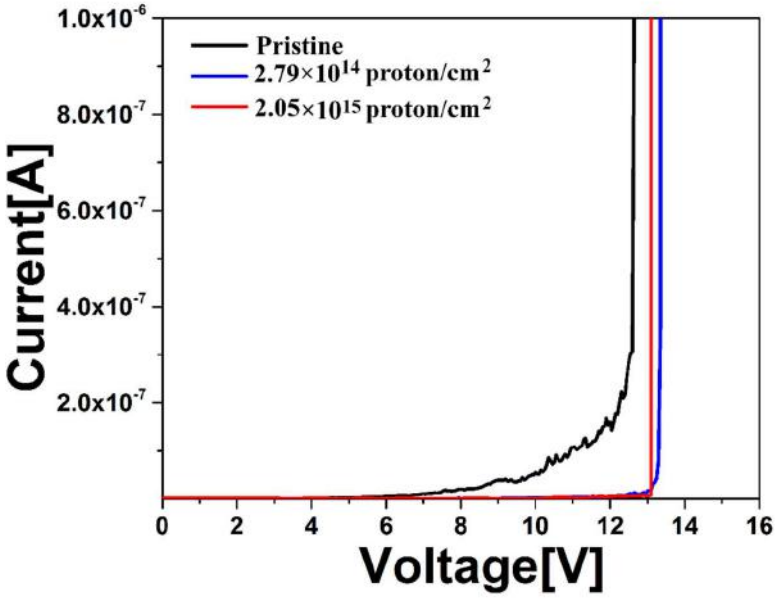

Figure 13. Forming voltages of Type 1 RRAM cells under two fluence conditions of 5 MeV protons.

ii) 60 keV protons

No Type 1 RRAM cells are formed and end up in the LRS even after being exposed to high 60-keV proton fluence (2×10^{15} cm^{-2}). The forming voltages for irradiated Type 1 RRAM cells are shown in Figure 14.

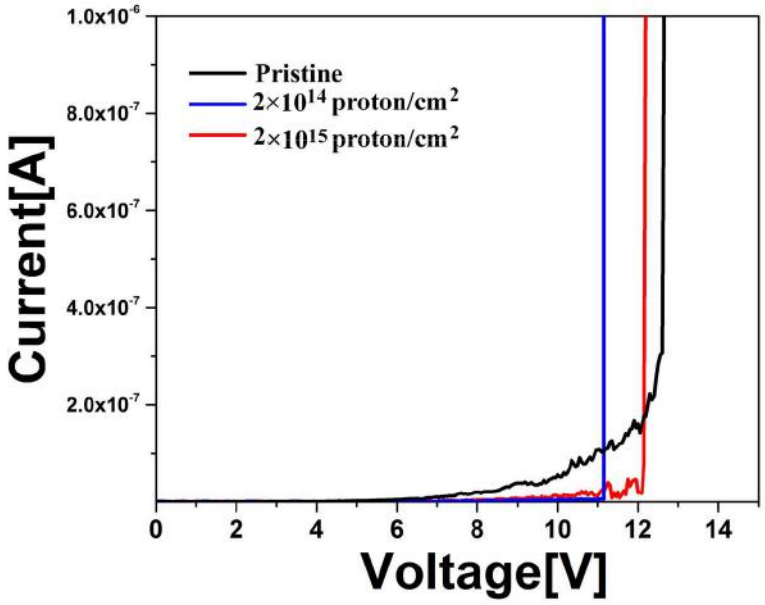

Figure 14. Forming voltages of Type 1 RRAM cells under two fluences for 60 keV proton irradiation.

No statistically different forming voltages were found in the forming voltage for pristine and irradiated. Type 1 RRAM cells.

Based on previous TRIM code calculation, 60 keV protons cause more displacement damage. However, it is clear that 60 keV protons do not affect the formation of a conduction path in the metal-oxide film.[16]

5.3.1.2 I-V Characteristics

i) 5MeV protons

I-V characteristics of 5 MeV proton-irradiated Type 1 RRAM cells are shown in Figure 15.

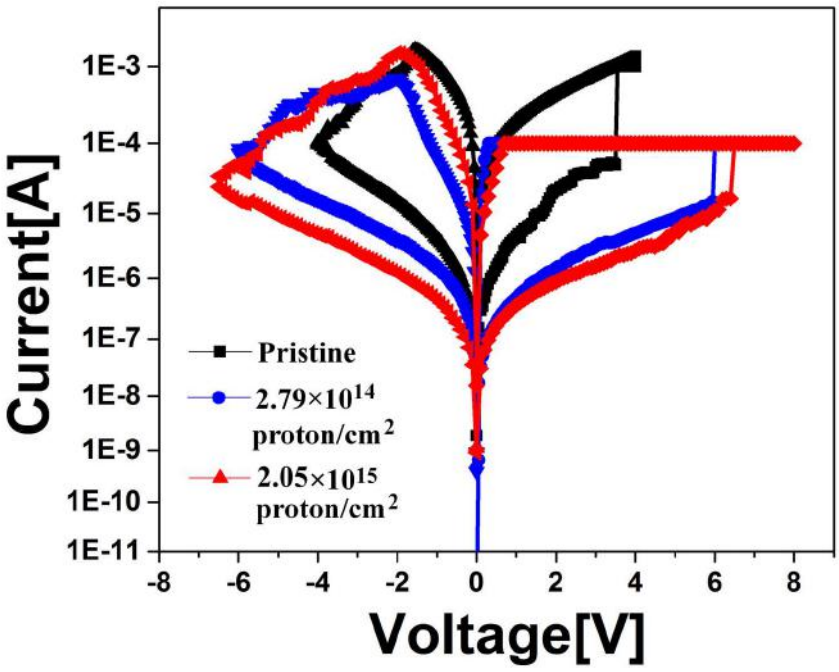

Figure 15. I-V characteristics of pristine Type 1 RRAM and Type 1 RRAM irradiated with two different proton fluences of 5 MeV protons.

The annealing effect appears as an increase in the resistance of the HRS. The proton-induced effects on Type 1 HfO_x RRAM devices agrees with the observations for blanket films that was shown in Section 5.2.1. In addition, the set voltages increased after proton irradiation. The largest increase in set voltage is from 3.5 to 7V. These shifts of set voltages may create problems in real device applications. First, the irradiated RRAM cannot achieve the set process at a fixed pulse voltage. Besides, even increasing the set voltage in the irradiated RRAM a little bit, a much large power is needed for the switching since the power is proportional to the square of the voltage.

ii) 60 keV protons

Figure 16 show the I-V characteristics of Type 1 RRAM cells irradiated with 60 keV protons.

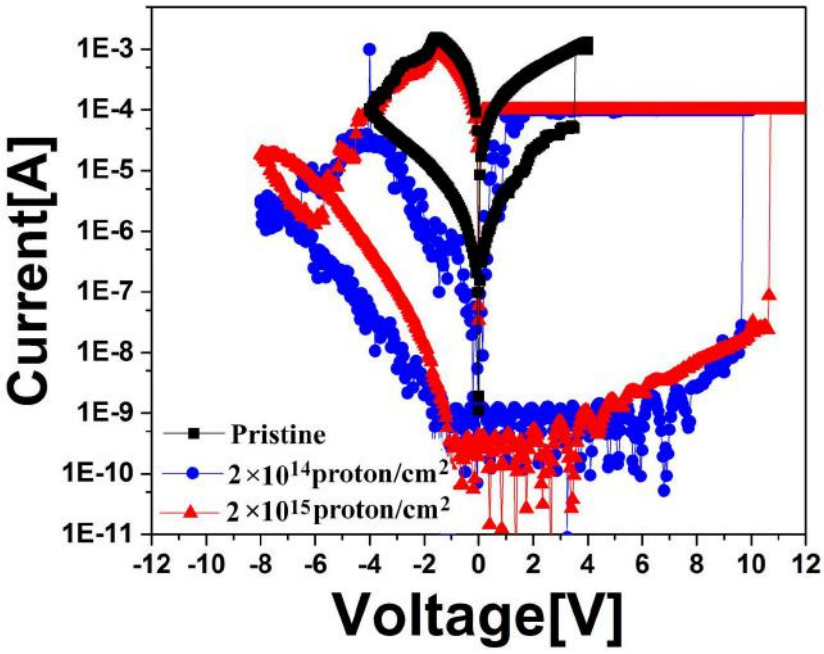

Figure 16. I-V characteristics of pristine Type 1 RRAM and Type 1 RRAM cells irradiated with 60 keV protons under two different fluences.

Based on the previous TRIM code calculation, more interaction for 60 keV protons should be found as is shown here. The annealing effect is more obvious with the 60 keV proton-irradiated Type 1 RRAM. In addition, the set voltage is higher than 10V after proton irradiation. These shifts of set voltages will also have the potential to create problems in real device applications.

5.3.1.3 Endurance

The endurance of pristine Type 1 RRAM and Type 1 RRAM irradiated with a high-proton fluence of approximately $2\times10^{15}cm^{-2}$ was measured. The proton energy for this measurement was 5MeV. The endurance test is designed to measure the number of pulsed-voltage cycles that can be applied to a RRAM device until it becomes unreliable.[17] Figure 17 shows the pulse cycle applied to the

Type 1 RRAM during the endurance test. Figure 18 is the result of this endurance test. From this figure, it is obvious that the endurance of Type 1 RRAM cells degrades after proton irradiation.

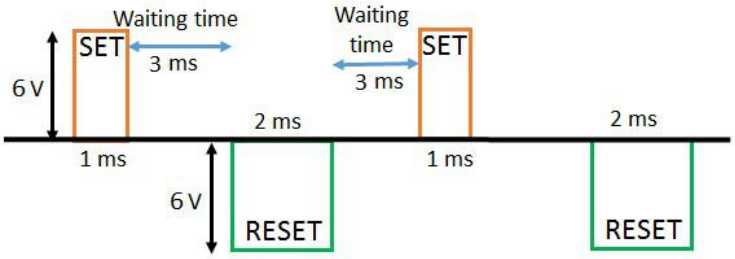

Figure 17. A pulsed voltage cycle applied to Type 1 RRAM for the endurance test. For every cycle, t_{cycle} = SET pulse width + RESET pulse width + waiting times = 9 ms.

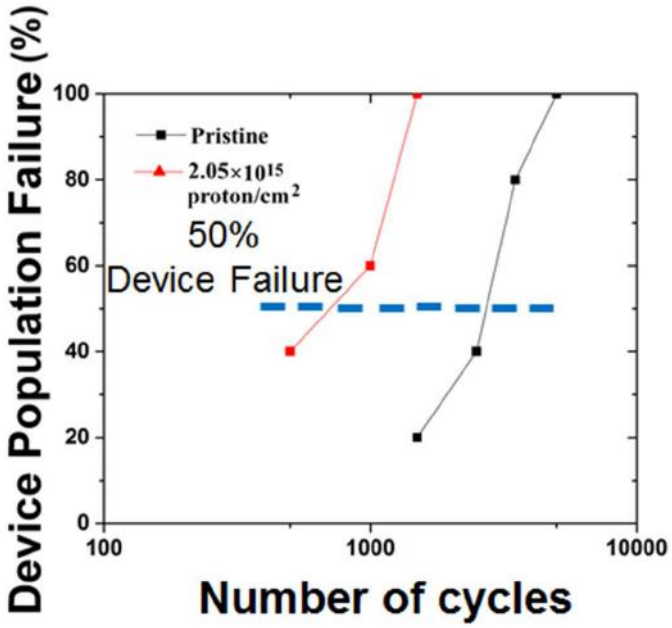

Figure 18. Endurance cycles for pristine and photon-irradiated Type 1 RRAM.

Summary of Section 5.3.1

From these observations, the following conclusions can be made. First, no Type 1 RRAM cells were formed that end up in the LRS state and no differences were found in the forming voltage after proton irradiation, even with different energies and fluences. Second, protons also anneal the HfO_x film used in Type 1 RRAM. Third, shift in values of the set voltage can be seen on the I-V characteristic of proton-irradiated Type 1 RRAM. In other words, it is more difficult to achieve the set process of the irradiated Type 1 RRAM. In addition, a consistent result from the endurance test is observed. The irradiated Type 1 RRAM lasts a significantly fewer number of switching cycles. The cause of the increase in set voltage and endurance degradation of irradiated Type 1 RRAM, is believed to be the result of similar atomic-structure changes in HfO_x caused by the proton irradiation as was observed in blanket HfO_2 films as described in Section 5.2.3

5.3.2 Sequential I-V characteristic measurements on irradiated Type 1 RRAM

In the previous section, the performance of Type 1 RRAM at different proton fluences was discussed. In this section, sequential I-V characteristic measurements on Type 1 RRAM cells at specific proton fluences are presented. This measurement was made to determine whether these proton-induced effects are permanent or recoverable after several switching cycles. For all measurements, the black lines are the first switching cycle, followed by red, blue and green lines.

i) 5 MeV protons

The sequential I-V characteristic measurements are shown in Figure 19. From these measurements, it shows that the influence of proton irradiation including “increasing in HRS resistance” and

"changes in set voltages" appear in every switching cycle. This indicates that this change may be the result of permanent damage to the Type 1 RRAM.

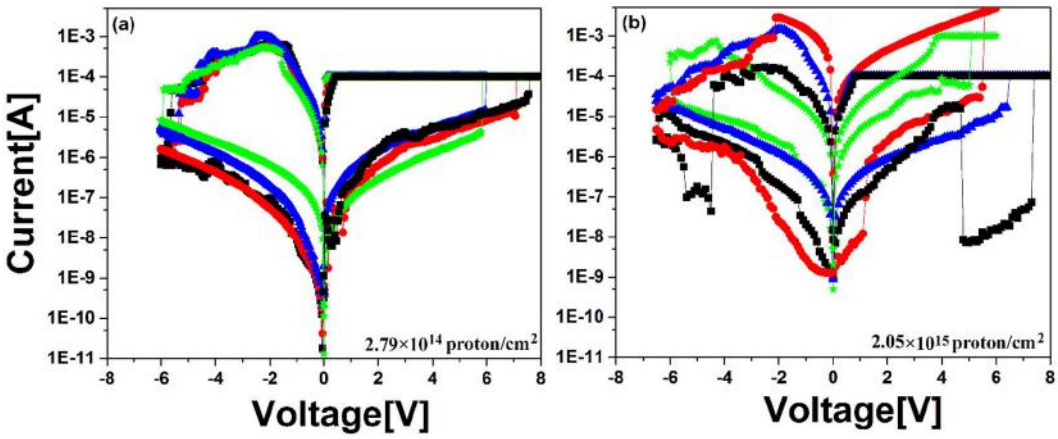

Figure 19. I-V characteristics of Type 1 RRAM cells irradiated by two proton fluences (a) 2.79 × 10^{14} protons/cm^2 and (b) 2.05 × 10^{15} protons/cm^2. The black lines are the first switching cycle, followed by red, blue, and green lines, respectively.

ii) 60 keV protons

The sequential I-V characteristic measurements are shown in Figure 20. The effects caused by 60 keV protons including "an increase in HRS resistance" and "changes to set voltages" may be regarded as permanent damage to the Type 1 RRAM.

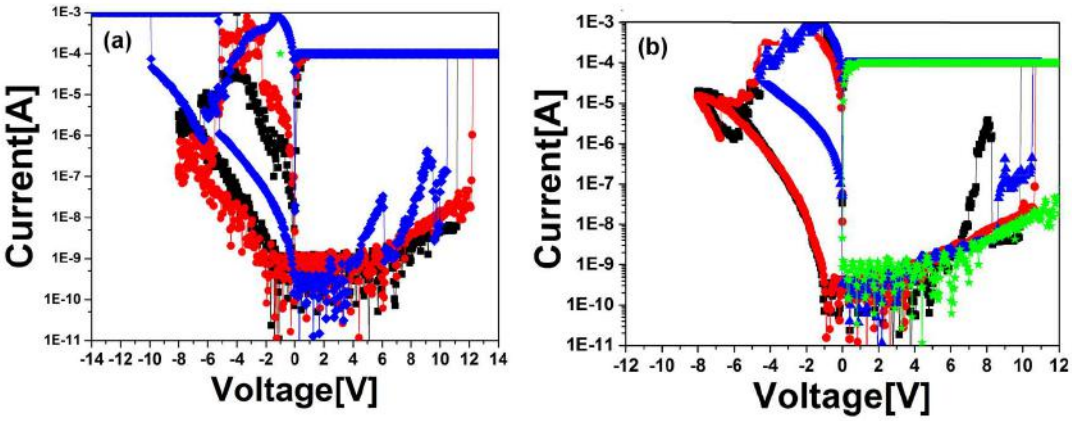

Figure 20. I-V characteristics of Type 1 RRAM cells irradiated with 60 keV protons with two fluences (a) 2×10^{14} protons/cm^2 and (b) 2×10^{15} protons/cm^2. The black lines are the first switching cycle, followed by red, blue, and green lines, respectively.

5.4 Effects of proton irradiation on Type 2 HfO_x RRAM

Here we discuss the effect of proton irradiation on Type 2 RRAM as shown in Figure 21.

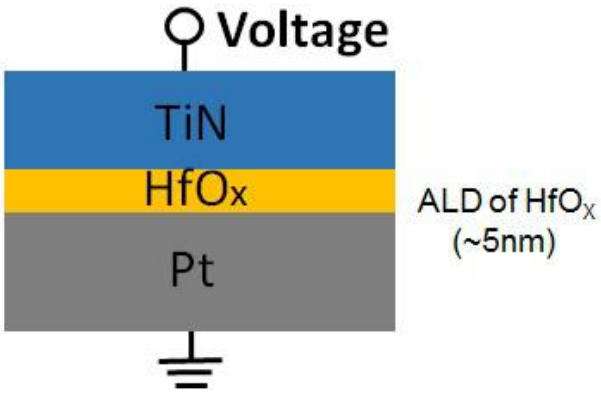

Figure 21. Schematic of the Type 2 RRAM cell. This RRAM cell is modified in two aspects: (1) Reduction of the thickness of the HfO_x, and (2) ALD fabrication of the HfO_x (~5 nm).

As described earlier, Type 2 RRAM has a thinner metal oxide than a Type 1 RRAM and a different fabrication process of the HfO_x film. The Type 2 RRAM was exposed to high proton fluence ($2 \times 10^{15} cm^{-2}$). The proton energy was either 5 MeV or 60keV as was the case for the Type 1 RRAM.

5.4.1 Type 2 RRAM Performance under proton irradiation

The forming rate, forming voltages, the resistances of the high resistance state (HRS), and the shift in set voltage of the irradiated Type 2 RRAM cells were measured. No Type 2 RRAM cells are formed and ended up in the LRS after exposing to either 5 MeV or 60 keV protons.

i) 5 MeV protons

Figures 22 and 23 shows the forming voltage and the I-V characteristics for pre-irradiated and post-irradiated Type 2 RRAM cells.

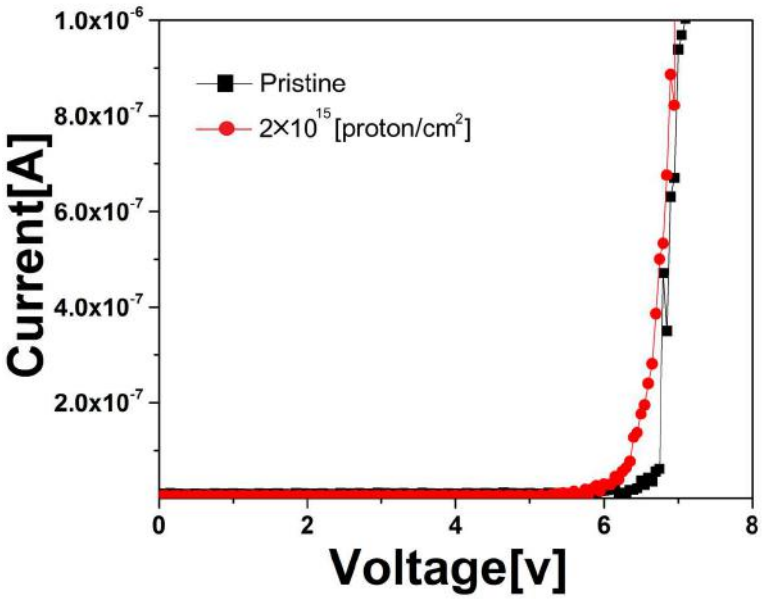

Figure 22. Forming voltages of Type 2 RRAM cells under 5 MeV protons.

The Type 2 RRAM showed no significant changes to the forming voltage and the I-V characteristics after 5 MeV proton irradiation. Hence, these Type 2 RRAM should be considered to be resistant to high proton fluence at this energy.

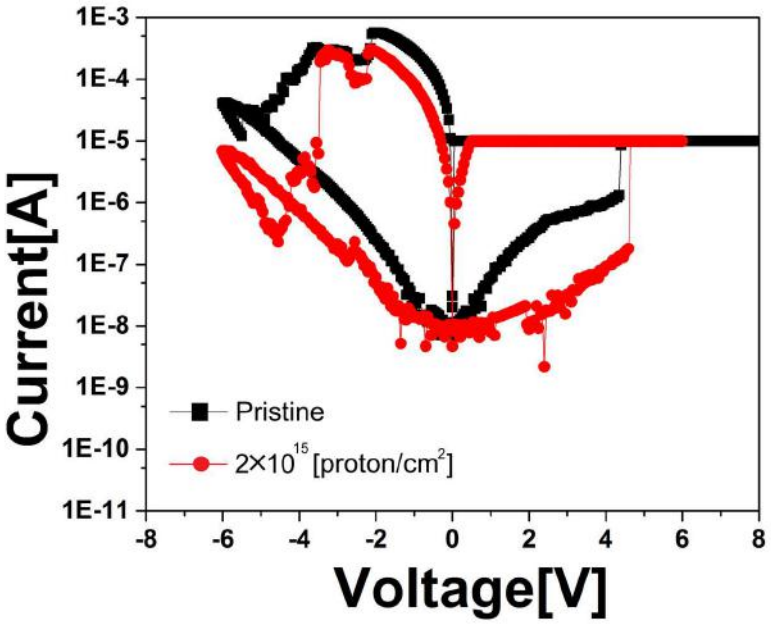

Figure 23. I-V characteristics of pre-irradiated and post-irradiated (5MeV) Type 2 RRAM cells.

ii) 60 keV protons

Figures 24 and 25 shows the forming voltage and the I-V characteristics for pre-irradiated and post-irradiated Type 2 RRAM cells.

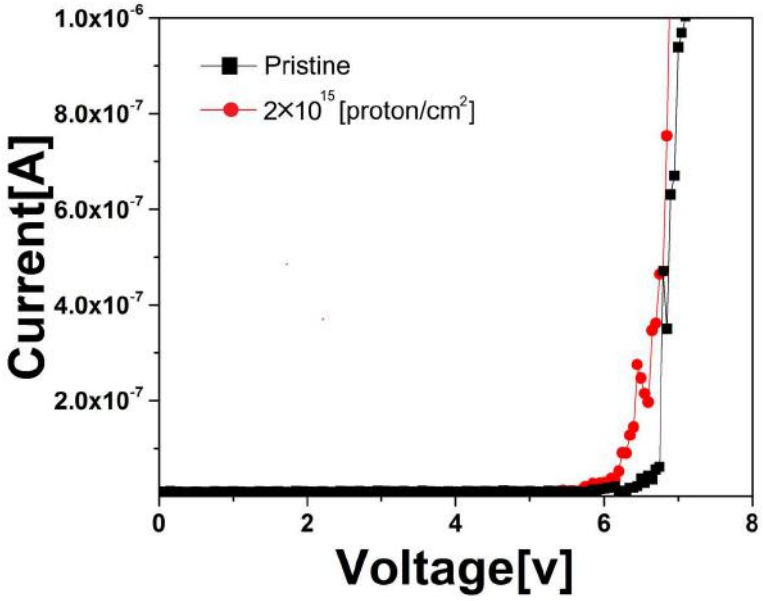

Figure 24. Forming voltages of Type 2 RRAM cells under 5 MeV protons.

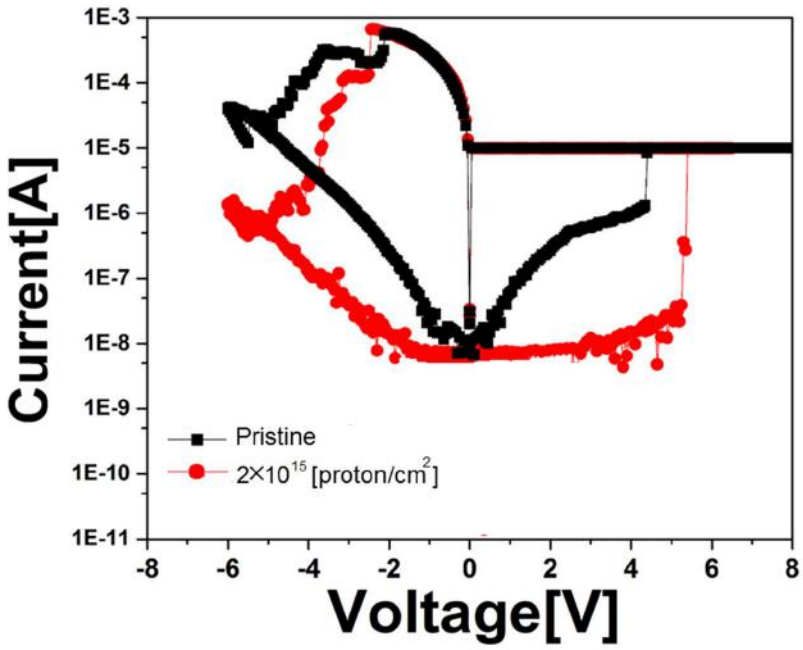

Figure 25. I-V characteristics of pre-irradiated and post-irradiated (60keV) Type 2 RRAM cells.

The Type 2 RRAM showed slight changes to the set voltage and the resistance of HRS after 60 keV proton irradiation. However, the changes were not very significant compared with the changes to Type 1 RRAM that was shown in Figure 16. Hence, the Type 2 RRAM again should be considered to be more resistant to high proton fluence at this energy than Type 1 RRAM.

5.4 Summary

A similar annealing effect was found in the defect concentrations and leakage currents of HfO_2 blanket films irradiated by 5 MeV and 60 keV protons. In addition, the annealing effects are more obvious in HfO_2 blanket films irradiated with 60 keV protons since more protons interact with the HfO_2 blanket films. The same annealing effect is also observed in the resistance of the HRS in Type 1 RRAM. Type 1 RRAM irradiated with 60 keV protons has a higher increase in the resistance of the HRS than Type 1 RRAM irradiated by 5 MeV protons.

On the other hand, no Type 1 RRAM was formed and exhibited the LRS and no changes were observed in the forming voltage of irradiated Type 1 RRAM. 60 keV protons have more interaction with the HfO_2 film within RRAM. However, these 60keV protons still could not generate a conduction path within the HfO_x film.

The shift in values of the set voltage can be seen on the I-V characteristic of Type 1 RRAM irradiated with 5 MeV and 60 keV protons. A degradation of the endurance was observed after 5 MeV proton irradiation. This is believed to be the result of atomic-structure changes in HfO_x caused by proton irradiation.

From sequential I-V characteristic measurements, the influence of proton (5MeV, 60keV) irradiation should be regarded as a permanent damage. Based on all the measurements about how

protons affect Type 1 RRAM, Type 2 RRAM is provided and is consider to be more resistant to high proton fluence than Type 1 RRAM.

REFERENCES

[1] D.Primetzhofer, "Electronic stopping power of hydrogen in a high-k material at the stopping maximum and below," *arXiv preprint arXiv:1308.0440* (2013).

[2] L. Timotijevic, I. Fetahovic, D. Lazarevic, and M. Vujisic, "Simulation of Proton Beam Effects in Thin Insulating Films," *Int. J.Photoenergy* **2013 (**2013).

[3] H. Ren, H. Sinha, A. Sehgal, M.T. Nichols, G.A. Antonelli, Y. Nishi and J. L.Shohet, "Surface potential due to charge accumulation during vacuum-ultraviolet exposure for high-k and low-k dielectrics," *Appl. Phys. Lett.* **97**, 072901 (2010).

[4] *Radiation hardening*, WWW Document (http:// en.wikipedia.org/wiki/Radiation_hardening)

[5] J. R. Srour, C. J. Marshall, and Paul W. Marshall, "Review of displacement damage effects in silicon devices," *IEEE Trans. Nucl. Sci.* **50**, 653 (2003).

[6] B. L. Gregory, "Injection-Stimulated Vacancy Reordering in p-Type Silicon at 76° K," *J. Appl. Phys.* **36**, 3765 (1965).

[7] *Interactions of ions with matter*, WWW Document (http://www.srim.org/)

[8] J. L. Barth, C. S. Dyer, and E. G. Stassinopoulos, "Space, atmospheric, and terrestrial radiation environments," *IEEE Trans. Nucl. Sci.* **50**, 466 (2003).

[9] C. Tschalär, "Straggling distributions of large energy losses," *Nucl. Instrum. Methods* **61**, 141 (1968).

[10] M. Tabib-Azar, D. Akinwande, G. E. Ponchak, and S. R. LeClair, "Evanescent microwave probeson high-resistivity silicon and its application in characterization of semiconductors," *Rev. Sci. Instrum.* **70**, 3083 (1999).

[11] S. Yu, X. Guan, and H.-S. Philip Wong, "Conduction mechanism of TiN/HfO_x/Pt resistive switching memory: A trap-assisted-tunneling model," *Appl. Phys. Lett.* **99**, 063507 (2011).

[12] W. S. Lau, "An Extended Unified Schottky-Poole-Frenkel Theory to Explain the Current-Voltage Characteristics of Thin Film Metal-Insulator-Metal Capacitors with Examples for Various High-k Dielectric Materials," *ECS J. Solid State Sci. Technol.* **1** N139 (2012).

[13] A. Benyagoub, "Swift heavy ion induced crystalline-to-crystalline phase transition in zirconia and hafnia: a comparative study," *Nucl. Instrum. Methods Phys. Res., Sect. B* **218**, 451 (2004).

[14] I. O. Usov, J. A. Valdez, J. Won, M. Hawley, D. J. Devlin, R. M. Dickerson, B. P. Uberuaga, Y.Q. Wang, C. J. Olson Reichhardt, G. D. Jarvinen, and K. E. Sickafus, "Irradiation effects in an HfO_2/MgO/HfO_2 tri-layer structure induced by 10MeV Au ion, " *Nucl. Instrum. Methods Phys. Res., Sect. B* **267**, 1918 (2009).

[15] N. V. Nguyen, A. V. Davydov and D. C. Horowitz, "Sub-bandgap defect states in polycrystalline hafnium oxide and their suppression by admixture of silicon," *Appl. Phys. Lett.* **87**, 192903 (2005).

[16] H.-S. Philip Wong, H-Y Lee, S. Yu, Y. S. Chen, Y. Wu, P-S Chen, B. Lee, F. T. Chen, and M-J Tsai, "Metal–oxide RRAM," *Proceedings of the IEEE* **100** 1951 (2012).

[17] Y. Y. Chen, R. Degraeve, S. Clima, B. Govoreanu, L. Goux, A. Fantini, G. S. Kar, G. Pourtois, G. Groeseneken, D. J. Wouters ,"Understanding of the endurance failure in scaled HfO_2-based 1T1R RRAM through vacancy mobility degradation," *Tech. Dig. IEEE Int. Electron Devices Meeting*, 20 (2012).

Chapter 6 - Conclusions and Future work

The goal of this work was to determine whether cosmic rays or other radiation affects RRAM. We looked into the radiation-induced effects on two types of RRAM cells and the mechanisms that cause these effects.

This work included two parts: (1) Measuring the radiation induced effects on HfO_2 thin films with the goal of identifying the damage-causing mechanisms of the radiation-induced effects on HfO_x RRAM. In addition, the degradation of the reliability of RRAM was also investigated. A comparison of the effects induced by different radiation sources was provided. (2) An RRAM cell with a thinner dielectric layer made by atomic layer deposition proved to be more damage resistant.

In the first section of this Chapter, a summary of the significant findings will be given. Then, recommendations for future work are provided.

6.1 Summary of Significant Results

6.1.1 Comparison of Neutron and Proton effects on Type 1 RRAM

For neutron irradiation, neutrons were generated in a light-water-moderated nuclear reactor where a continuous neutron spectrum is present including thermal, epithermal and fast neutrons. In this work, the highest neutron fluences were:

Thermal (<1eV)	Epithermal (>1eV, <1MeV)	Fast (>1MeV)	
1.33×10^{14}	3.84×10^{12}	1.76×10^{13}	(neutrons/cm^2)

At this neutron fluence, 90 % of the RRAM cells are formed with neutron irradiation alone, and end up in the low resistance states (LRS). For any unformed neutron-irradiated RRAM cells, lower voltages were needed to form the cell. In addition, the resistance of the high resistance state (HRS) increased after neutron irradiation. From the sequential I-V characteristic measurements of the irradiated RRAM cells, the influence of neutron irradiation disappears after several switching cycles.

The forming process generated by neutrons, the reduced forming voltage for unformed RRAM and the increase in HRS resistance for neutron-formed RRAM, can be regarded as the results of the displacement effects of neutrons, followed by anneal enhanced by electrons generated during ionization process. These effects are consistent with the measurements made on the neutron-irradiated ultra-thin HfO_2 blanket films.

In addition, the resistance of the low-resistance state (LRS) exhibited very little dependence on area. This may indicate that some oxygen vacancies in a large-area RRAM are formed away from the primary conduction path.

However, protons with different energies (5MeV, 60keV) do not result in any formed RRAM and no change in the forming voltage was observed at a fluence level up to 2×10^{15} protons/cm^2. A similar increase in the resistance of HRS is also observed on proton-irradiated RRAM. From the sequential I-V characteristic measurements of the irradiated RRAM cells, the influence of proton irradiation lasts after several switching cycles.

Therefore, for protons, no obvious displacement effects are observed. The increase in the HRS which is an annealing effect by protons that is similar to that for neutrons, however, was observed.

The shifts in values of the set voltage can be seen on the I-V characteristics of both neutron-irradiated and proton-irradiated RRAM cells. Degradation of endurance was also observed on both neutron-irradiated and proton-irradiated RRAM cells. This is believed to be the result of atomic-structure changes in HfO_x caused by the irradiation.

A table is shown below to list the neutron and proton induced effects on Type 1 RRAM.

	Neutron	Proton
Formed after irradiation	✓	✗
Increase in HRS (anneal effect)	✓	✓
Shift in set/reset voltage	✓	✓
Endurance degradation	✓	✓

Table I. Summary of neutron and proton effects on Type 1 RRAM.

6.1.2 A modified RRAM (Type 2) to increase radiation hardness

The Type 2 RRAM device was proposed as a solution, based on previous measurements and the literature. The Type 2 RRAM cells were modified in two aspects: (1) Reduced thickness of the metal-oxide film within the RRAM, and (2) Use of atomic layer deposition (ALD) to deposit the HfO_x film.

There were no Type 2 RRAM cells that are formed ending up in the LRS after neutron and proton irradiation. There was no significant alternation in forming voltage and I-V characteristics after

neutron and proton irradiation. Thus the Type 2 RRAM have been shown to be resistant to high fluence neutron and proton irradiation.

A table is shown below to list the neutron and proton induced effects on Type 2 RRAM.

	Neutron	Proton
Formed after irradiation	✗	✗
Increase in HRS (anneal effect)	✗	✗
Shift in set/reset voltage	✗	✗

Table II. Summary of neutron and proton effects on Type 2 RRAM.

6.2 Recommendations for Future Work

Measurements of radiation-induced effects on RRAM and the damage mechanisms have been presented in this work. A new RRAM design was also proposed to increase radiation hardness. These results act as a foundation for exciting future work.

In this section, a number of recommendations for future work will be provided as possibilities to extend the work.

I-V characteristics of neutron and proton irradiated RRAM cells were measured and discussed in the previous section. We found that leakage current in the high-resistance state would decrease after neutron irradiation. However, this neutron-induced effect was not permanent.

For pristine RRAM, the conduction mechanism was dominated by defect-assisted tunneling. For neutron-irradiated RRAM, temperature-dependent I-V characteristics should be performed to determine the dominant conduction mechanism.

There are several mechanisms that have been proposed[1,2]for electronic transport in RRAM. Most of them can be categorized into a thermionic process that involves thermal activation and a tunneling process that does not involve thermal activation. It should be possible to infer the dominant electronic transport in the neutron irradiated RRAM from the temperature dependent I-V characteristics.

In addition, measurements of single event upsets (SEU)[3] in RRAM before, during and after irradiation is also a very important task that must be undertaken.

REFERENCES

[1] H.-S. Philip Wong, H-Y Lee, S. Yu, Y. S. Chen, Y. Wu, P-S Chen, B. Lee, F. T. Chen, and M-J Tsai, "Metal–oxide RRAM," *Proc. IEEE* **100**, 1951 (2012).

[2] S. Yu, X. Guan, and H.-S. Philip Wong, "Conduction mechanism of TiN/HfO_x/Pt resistive switching memory: A trap-assisted-tunneling model," *Appl. Phys. Lett.* **99**, 063507 (2011).

[3] A. Paccagnella, S. Gerardin and G. Cellere, "Radiation damage on dielectrics: Single event effects," *J. Vac. Sci. Technol. B* **27**, 406 (2009).